Department of Physics and Astronomy

University of Heidelberg

Bachelor thesis

in Physics

submitted by

Sabine Rockenstein

born in Hechingen (Germany)

September 2019

Active Carrier-Envelope Phase Stabilisation of Ultrashort Laser Pulses

This Bachelor thesis has been carried out by

Sabine Rockenstein

at the

Max Planck Institute for Nuclear Physics

under the supervision of

Prof. Dr. Thomas Pfeifer

Abstract

An f-2f-interferometer was set up to measure the carrier-envelope phase (CEP) of ultrashort laser pulses. A control loop was established to stabilize the CEP in order to enable future experiments with minimized fluctuations of the CEP. Properties of this PI-control-loop were observed and suitable control values were found; the regulation of the CEP to a desired value with a standard deviation of as low as 163 mrad was reached. As the generation of High Harmonics (HHG) is highly sensitive to the CEP of the fundamental pulse, the control loop was tested by determining the harmonic spectrum of attosecond pulses generated for different CEPs. It was found that the energy of harmonic orders in the cutoff region shifts depending on the CEP, which corresponds to the theoretical expectations.

Zusammenfassung

Zur Detektion der Träger-Einhüllenden-Phase (CEP) von ultrakurzen Laserpulsen wurde ein f-2f-Interferometer aufgebaut. Zur Stabilisierung der CEP wurde eine Kontrollschleife eingerichtet, die eine Regelung der CEP mit einer Standardabweichung von 163 mrad auch über längere Zeit erlaubt. Diese soll zukünftig Experimente mit reduzierter Fluktuation der CEP ermöglichen. Eigenschaften des aufgebauten PI-Regelkreises wurden untersucht und geeignete Regelparameter zur Stabilisierung gefunden. Da die Erzeugung von Hohen Harmonischen (High Harmonic Generation, HHG) stark von der CEP abhängt, wurde die Regelung durch die Aufnahme der harmonischen Spektren von in Argon erzeugten Attosekundenpulsen bei verschiedener CEP getestet. Es wurde eine von der CEP abhängige Energieverschiebung der Harmonischen im Cutoff-Bereich festgestellt, die den theoretischen Erwartungen entspricht.

Contents

Motivation

For ultrashort laser pulses in the femtosecond range ($1fs = 10^{-15}s$), which consist of only a few oscillations of the electric field, the so called carrier-envelope phase (CEP, φ_{CE}) becomes important. The carrier-envelope phase is defined as the phase difference between the maximum of the oscillating electric field ("carrier") and its envelope and influences the shape of the pulse crucially, like shown in figure 1. Especially the peak intensity is determined by the CEP.

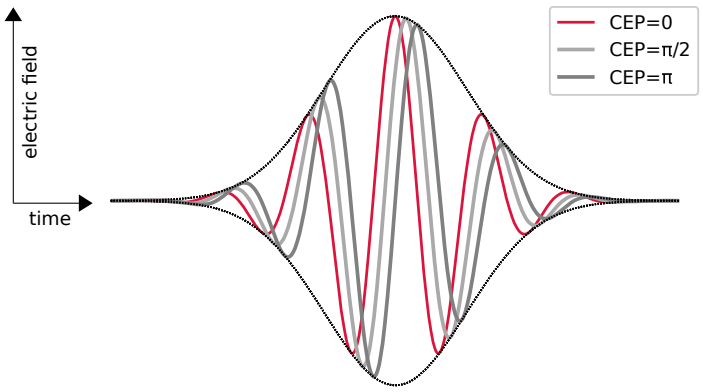

Figure 1: *An ultrashort laserpulse. The carrier (red) is the oscillating electric field with a frequency ω_c, that is enveloped by a gaussian (black). For the red pulse, the maxima of carrier and envelope match, so $\varphi_{CE} = 0$. The carriers depicted in gray lines are translated in time against the red pulse. The CEP is defined as the resulting phase difference between these pulses and the red pulse.*

For experiments that make use of ultrashort pulses, like High Harmonic Generation (HHG), it is important to determine and control the CEP to avoid fluctuations in the behaviour of the pulses. Through High Harmonic Generation, it is possible to produce even shorter pulses in an attosecond range ($1as = 10^{-18}s$), whose duration is in the same order of magnitude as the movement of electrons in an atom and which can be used for doing spectroscopic experiments and observing the dynamic of electrons. As the generation of high harmonics is quite sensitive to a change in CEP, stabilization of this parameter is a necessary prerequisite for getting reliable experimental results.
This thesis describes the implementation of an f-2f-interferometer and a control loop to measure and stabilize the CEP.

1 Ultrashort laser pulses and measurement of the carrier-envelope phase

This chapter is an introduction into the mathematical description of ultrashort laser pulses. In particular, the carrier-envelope phase is introduced and its effects on the temporal evolution of a femtosecond pulse is explained. Also, the theory behind an f-2f-interferometer, that is an often used instrument to determine the carrier-envelope phase of pulses, is shown and the properties of the specific f-2f-interferometer that was set up as a part of this thesis are described.

1.1 Definition of the CEP

The electric field $E(t)$ of a laser pulse at a certain position can be described as

$$E(t) = \varepsilon(t) exp(i\varphi(t)), \tag{1}$$

where $\varepsilon(t)$ is the envelope of the pulse, often a Gaussian or some even power of a cosine-function, and $\varphi(t)$ is the absolute phase of the pulse. This temporal phase can be Taylor-expanded as

$$\varphi(t) = \sum_{n=0}^{\infty} \frac{1}{n!} \frac{\partial^n \varphi}{\partial t^n}\bigg|_{t_0} (t - t_0)^n = \varphi_{CE} + \omega_c(t - t_0) + \mathcal{O}((t - t_0)^2). \tag{2}$$

The constant φ_{CE} is the carrier-envelope phase. It leads to a shift of the carrier with respect to the envelope; explicitly φ_{CE} defines the phase difference between the maxima of both, the envelope and the carrier (see figure 1). ω_c is the frequency of the carrier.

After a Fourier transformation, a pulse can similarly be described in the frequency domain as [1]

$$\tilde{E}(\omega) = \frac{1}{\sqrt{2\pi}} \int_{-\infty}^{\infty} E(t) exp(-it\omega) dt = \tilde{\varepsilon}(\omega) exp(i\varphi(\omega)). \tag{3}$$

The term $\varphi(\omega)$ is the so called spectral phase, that can be Taylor-expanded as well:

$$\varphi(\omega) = \sum_{n=0}^{\infty} \frac{1}{n!} \frac{\partial^n \varphi}{\partial \omega^n}\bigg|_{\omega_0} (\omega - \omega_0)^n \ = \varphi_{CE} + \tau_0(\omega - \omega_0) + \mathrm{GDD}(\omega - \omega_0)^2 + \mathcal{O}((\omega - \omega_0)^3). \tag{4}$$

Here, φ_{CE} is a constant offset again. $\tau_0 = \frac{\partial \varphi_0}{\partial \omega}$ is the group delay, which causes a shift of the whole pulse in time. The second-order term is the group delay dispersion (GDD), that adds a linear chirp to the pulse [1].

A pulse train consists of single ultrashort laser pulses that can be described like in equation 1 and are repeated after integer multiples of the cavity round trip time T_R. So for mode-locked lasers, the repetition rate of the emitted pulses is $f_{rep} = \frac{1}{T_R} = \frac{\omega_{rep}}{2\pi}$. Inside the cavity, the carrier propagates with the phase velocity $v_p = \frac{\omega}{k}$ and the envelope propagates with the group velocity $v_g = \frac{d\omega}{dk}$. In a first attempt to understand the temporal evolution of the pulse, it is assumed that these velocities are the same. This is not the case in general, as both of them depend on the propagation distance and on the dispersion of the material they are propagating through. With equal velocities, the absolute phase of the pulse would not change with time. So for $v_g = v_p$ a pulsetrain would, following the notation and the structure of [2] for the rest

of this derivation, be a convolution of one single pulse with a delta distribution repeated after every T_R:

$$E_{train}(t) = \varepsilon(t)exp(i\varphi(t)) \circledast \sum_{n=-\infty}^{\infty} \delta(t - nT_R), \tag{5}$$

where $\circledast$ is the symbol for a convolution, and by definition it is clear that a convolution with a delta function gives back the original function shifted in the direction of x:

$$(f \circledast g)(x) = \int_{-\infty}^{\infty} f(y)g(x-y)dy. \tag{6}$$

In the frequency domain, the same pulse train would be described by a so called frequency comb

$$\tilde{E}_{train}(f) = \tilde{\varepsilon}(f - f_c) \sum_{n=-\infty}^{\infty} \delta(f - nf_{rep}). \tag{7}$$

A frequency comb is a model to describe all frequencies contained in a pulse. As for mode-locked lasers these frequencies are well defined as multiples of the repetition rate $f_{rep} = \frac{1}{T_R}$, there are equidistant sharp lines, separated by f_{rep}, the so called "teeth". These are enveloped by $\tilde{\varepsilon}(f - f_c)$, where $f_c = \frac{\omega_c}{2\pi}$. An example of a frequency comb can be found in figure 2.

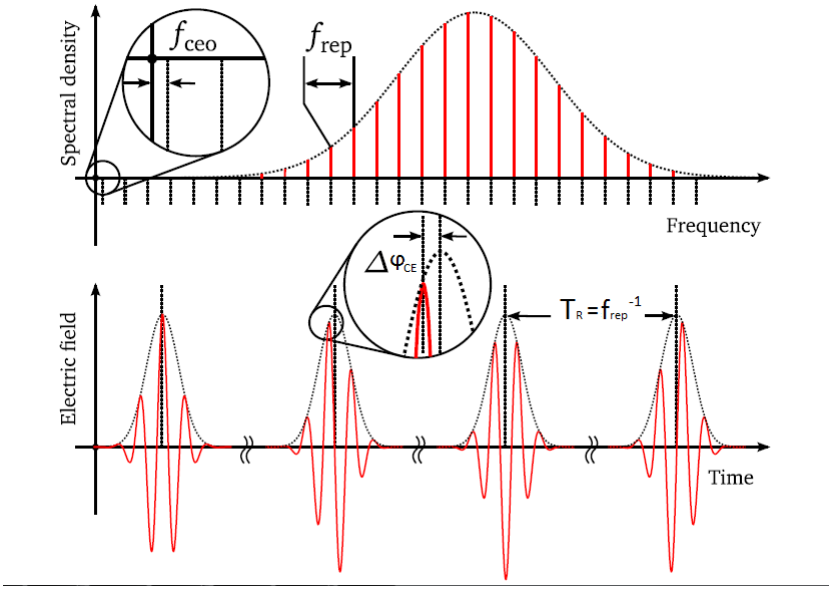

Figure 2: *In the upper half of the illustration a frequency comb is shown. In the lower half the corresponding pulses in the time domain are depicted. The red lines are the oscillating electric field and the black dotted lines are the carrier. As $f_{CEO} \neq 0$, φ_{CE} is changing for two consecutive pulses. The pulse shape changes visibly. Taken from [3], modified.*

To look at a more general case, where $v_g \neq v_p$, the Fourier components experience a phase shift Ψ as the carrier is delayed against the envelope. If the pulse with a wave number k propagates through a dispersive medium of length L with an index of refraction $n(\omega)$ that depends on the frequency, the group velocity can be derived as follows:

$$\Psi(\omega) = -\int_0^L k(\omega, x)dx = -\int_0^L \frac{n(\omega)\omega}{c}dx \tag{8}$$

$$\frac{1}{v_g} = \left(\frac{d\omega}{dk}\right)^{-1} = \frac{1}{c}\left(\frac{dn(\omega)}{d\omega}\omega + n(\omega)\right) = \frac{1}{v_p} + \frac{dn(\omega)}{d\omega}\frac{\omega}{c}. \tag{9}$$

The group-phase-offset $\Delta\varphi_{GPO}$

$$\Delta\varphi_{GPO} = -\omega\int_0^L (\frac{1}{v_g} - \frac{1}{v_p})dx = \int_0^L \frac{\omega^2}{c}\frac{dn(\omega, x)}{d\omega}dx \tag{10}$$

is the lag between carrier and envelope over the length of the medium caused by first-order dispersion. The change of the carrier envelope phase φ_{CE} per round trip in the cavity is exactly the group-phase-offset $\Delta\varphi_{GPO}$ mod 2π. This follows from the periodicity of the trigonometric functions, so a CEP of $\frac{\pi}{2}$ is the same as one of $\frac{5\pi}{2}$. The respecting carrier-envelope offset frequency f_{CEO} follows to be

$$f_{CEO} = \frac{1}{2\pi}\frac{\Delta\varphi_{GPO}}{T_R}. \tag{11}$$

By using this, equations 5 and 7 can therefore be expressed more generally as

$$E_{train}(t) = \varepsilon(t)exp(i\omega_c t + i\omega_{CEO}t) \circledast \sum_{n=-\infty}^{\infty} \delta(t - nT_R) \tag{12}$$

$$\tilde{E}_{train}(f) = \tilde{\varepsilon}(f - f_c) \sum_{n=-\infty}^{\infty} \delta(f - nf_{rep} - f_{CEO}). \tag{13}$$

The phases of the pulses were only considered up to the first order. The frequency comb is shifted by f_{CEO} and changes in this offset frequency translate the whole frequency comb on the frequency axis.

The more illustrative way of thinking about the CEP is by seeing it as the phase difference between the maximum of the envelope and the one of the carrier, like it was defined in the first paragraph of this section. In figure 2, there are pulses depicted for different CEPs and it is apparent that the pulse shape changes from pulse to pulse. For experiments where the peak intensity of pulses plays a role, it is required to keep the CEP at a constant value to avoid unwanted effects resulting from this change.

One widespread technique to measure the CEP is by using an f-2f-interferometer. The general function of such an interferometer as well as the specific one built up and used in this thesis will be described in the next section.

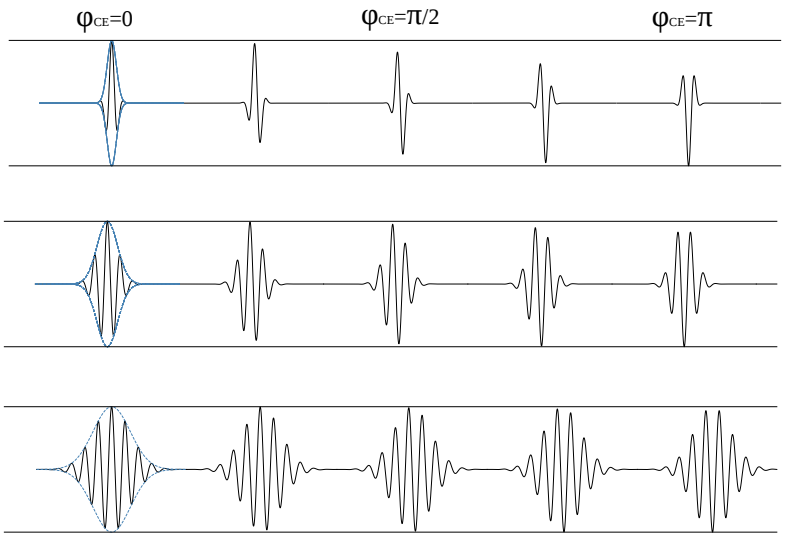

Figure 3: *Ultrashort laserpulses with changing CEP. Depicted is the temporal evolution of the electric field (black lines) at one fixed position in arbitrary units. For better intuition, for the first pulse in each row ($\varphi_{CE} = 0$), the gaussian envelope is shown as well (blue line). The change in CEP from pulse to pulse is $\pi/4$. The pulse duration of the pulses in the first row is 1/5 of the ones in the second row and 1/15 of the ones in the last row. The horizontal black lines are located at the position of the maximum of the envelope.*

1.2 f-2f-interferometer

When observing the temporal change of a system, events even shorter than the movement happening are required in order to resolve the dynamic evolution. For example, when looking at the wing beat of a hummingbird, the movement of the wings can not be seen with naked eyes. Only a blurred motion is visible as the hummingbird moves its wings with a frequency of more than 50 Hz [4] and the temporal resolution of human visual perception is around 25 frames per second [5]. But with the help of a camera with an exposure time that is short enough, it is possible to take sharp pictures.

Consequently, it is difficult to observe events in the femtosecond region, because the duration of the event is much to short to be registered by electronics, which act on a nano- to picosecond scale. A common strategy to observe such ultrafast events is to use a copy of the pulse which undergoes a non-linear change and to have a so called self-referencing measurement by comparing the original pulse to the changed one. This principle is the underlying concept of an f-2f-interferometer. As the name implies, in an f-2f-interferometer, out of the fundamental pulse there is light of twice the frequency generated by second harmonic generation (SHG). This happens in a $\beta - BaB_2O_4$ (BBO) crystal or in another nonlinear crystal. If the original pulse and the frequency-doubled one have a spectral overlap, they interfere and this interference pattern can be detected by a spectrometer.

Every frequency that occurs in the original pulse can be described as [2]

$$f_m^{fund} = mf_{rep} + f_{CEO},\ m \in \mathbb{N}. \tag{14}$$

The frequencies in the frequency doubled pulse therefore can be derived as

$$f_m^{SHG} = 2mf_{rep} + 2f_{CEO},\ m \in \mathbb{N}. \tag{15}$$

If the spectrum includes at least one octave, there will be at least one k for which also light of the frequency $f_{2k} = 2kf_{rep} + f_{CEO}$ is contained in the fundamental spectrum. In the second harmonic spectrum, there is a frequency of $f_k = 2kf_{rep} + 2f_{CEO}$ contained. So in the region of spectral overlap, where both, fundamental light as well as second harmonic light, are included, the carrier-envelope offset frequency can be determined out of the overlying frequency combs. This is because

$$2f_m - f_{2m} = f_{CEO}. \tag{16}$$

How exactly one can experimentally obtain the carrier offset frequency from the interference pattern is shown in section 1.2.3. First, the theory behind second harmonic generation and the general setup of the interferometer will be explained.

1.2.1 Second Harmonic Generation

Second Harmonic Generation is a nonlinear optical process, which means it can only occur if the polarization P in the medium does not only depend linearly, but also on higher orders on the irradiated electric field

$$P(E) = p^{(1)} + p^{(2)} + p^{(3)} + ... = c_0(\chi^{(1)}E + \chi^{(2)}E^2 + \chi^{(3)}E^3 + ...). \tag{17}$$

c_0 is the speed of light in vacuum and $\chi^{(n)}$ is the susceptibility of n^{th} order. The quantity of $\chi^{(n)}$ depends on the exact nature of the medium, like symmetry properties [6].
Assuming a continuous wave with only one frequency, the electric field at a specific position looks like

$$E(t) = E_0 cos(\omega t). \tag{18}$$

This assumption does not change the principle for a pulsed electric field, it only simplifies the following calculations. The second order term of the polarisation is then equal to

$$p^{(2)} = \frac{1}{2}c_0\chi^{(2)}[E_0^2(1 + cos(2\omega t)] \tag{19}$$

So you can see from this formula that light of exactly double the original frequency appears. If a pulse consisting of more frequencies is assumed, some extra terms appear: there is frequency mixing, like addition and subtraction of frequencies in the trigonometric term. But as we only focus on second harmonics here, and these effects cancel each other out with time if the phase matching is not correct, they will be neglected. Details on phase matching can be found in the next paragraph. The intensity of the SHG-light is proportional to the squared intensity of the fundamental light (compare to equation 17)

$$I(2\omega) \propto I^2(\omega) \tag{20}$$

and depends also on the phase matching.
Phase matching means, that the momentum of all photons involved in a process has to be conserved [6]:

$$\vec{k}(2\omega) = 2\vec{k}(\omega) \Rightarrow v_p(2\omega) = v_p(\omega). \tag{21}$$

The light generated in the BBO is polarized perpendicular to the fundamental light. The BBO crystal is birefringent. For birefringent crystals, the refractive index depends on the polarisation of the light. BBO crystals also are biaxial crystals, that means there are three mutually orthogonal principal axes associated with different refractive indices [7]. So in order to get the same phase velocity $v_p = \frac{c_0}{n(\omega)}$ for both waves, the crystal has to be rotated to an angle where the indices of refraction are the same for the fundamental light of frequency ω_c and the frequency doubled light of $2\omega_c$. Only if such an angle is found, light of twice the fundamental frequency is generated, because otherwise the waves would interfere destructively.

1.2.2 CEPset$^{\mathbf{TM}}$ interferometer

The used f-2f-interferometer consists mainly of a BBO-crystal, where second harmonic generation takes place and a spectrometer detecting the resulting interference pattern of the fundamental beam and the second harmonic beam. In figure 4, the whole setup can be seen.

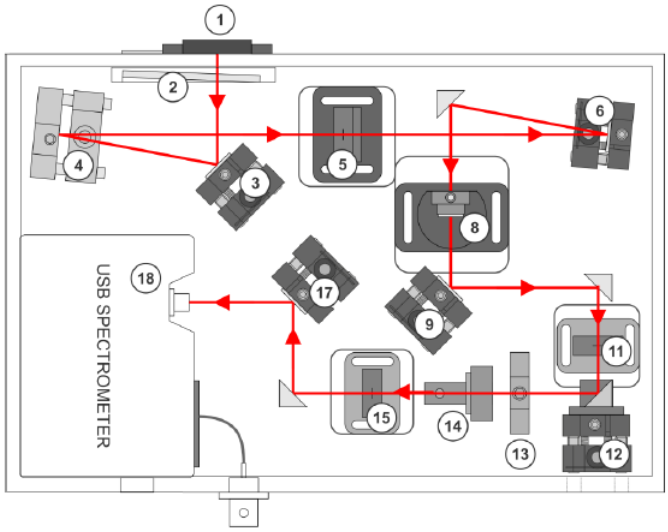

Figure 4: *The FEMTOLASERS^{TM} CEPset^{TM} f-2f-interferometer. The components are described in the text. Taken from [8], modified.*

By varying the iris (1) and the variable neutral-density (ND) filter (2), whose optical density can be changed in a range of 0.04 to 4.00, one can influence the intensity of the light getting inside the interferometer. A neutral density filter is characterized by reducing the intensity of all wavelengths of light equally by the amount of the optical density, which is the common logarithm of the fraction of the transmitted intensity over the incident intensity.
Because a spectrum of at least one octave is required to measure the CEP (see section 1.2.3),

a sapphire plate (5) is necessary to broaden the spectrum. At the sapphire plate, white light generation takes place. This light is focused onto the BBO-crystal (8) by a focusing mirror. The position of the BBO can be changed, so that the BBO, which is 500 μm thick, is in the exact position of the focus. The angle of the BBO with respect to the beam propagation direction can (and has to) be changed, until blue light is detected afterwards. The fundamental beam has typically a wavelength somewhere between 600 nm and 900 nm at the position where the CEP is measured. The central frequency is 750 nm and the full-width at tenth maximum (FWTM) is 300 nm. A sample spectrum can be seen in 12. The BBO is dimensioned for doubling the highest wavelengths of the Ti:Sapphire-spectrum. The frequency doubled beam's wavelength therefore lies in a blue wavelength region. The exact wavelength of the emitted SHG-light depends on the phase matching and can be changed by changing the angle of the BBO in respect to the beam. So there is an overlap in the spectrum of the two beams possible for these wavelengths. An interference pattern can be detected as a result of the superposition of these beams. The next chapter shows how this pattern depends on the CEP.

After the BBO, the fundamental light as well as the frequency doubled light pass a polarizing beam splitter (PBS, 14). As the two beams are polarised perpendicular to each other, the ratio of the intensity of the two beams can be varied by rotating the PBS. If the BBO-crystal is removed, there is an angle where no light can be detected after the polarizing beam splitter, which verifies the linear polarization of the incoming fundamental pulses. At an angle perpendicular to this polarization, and with inserted and correctly aligned BBO crystal, blue light in a wavelength-region of about 450 nm is visible. For optimizing the signal detected by the spectrometer, one has to set an angle of the PBS in between those maxima in order to detect the desired interference fringes and to improve the contrast of the signal. To avoid saturation of the spectrometer, a ND filter (13) with an optical density of 1 has been implemented right before the PBS. The beam is focused into an Ocean Optics Flame spectrometer (18) by a lens (15). In order to couple into the spectrometer, there are two steering mirrors (12,17) available.

1.2.3 Determination of the CEP out of interference fringes

The electric field of the incoming light pulse and the one of the frequency doubled light pulse add to each other linearly. The spectrometer detects an intensity spectrum, which is proportional to the square of the electric field, depending on the wavelength. A sample spectrum is depicted in figure 5. From this pattern, the CEP can be determined. At this point, it is important to mention that the exact carrier-envelope phase cannot be measured. Nonlinearity and material dispersion cause changes in the CEP which cannot be measured with the f-2f-interferometer [3]. So there is always an unknown offset on the values and only changes in CEP can be detected. For all the CEP-plots in this thesis, the values are only relative to an arbitrarily chosen CEP of unknown value.
In equation 1, the electric field of a laser pulse was described in dependence of time. Now, it will be described in the frequency domain again. If every constant and every term depending on $\omega - \omega_c$ is included in $\tilde{\varepsilon}$, it looks like

$$E_{fund}(\omega) = \tilde{\varepsilon}(\omega - \omega_c) exp(i\varphi_{CE}). \tag{22}$$

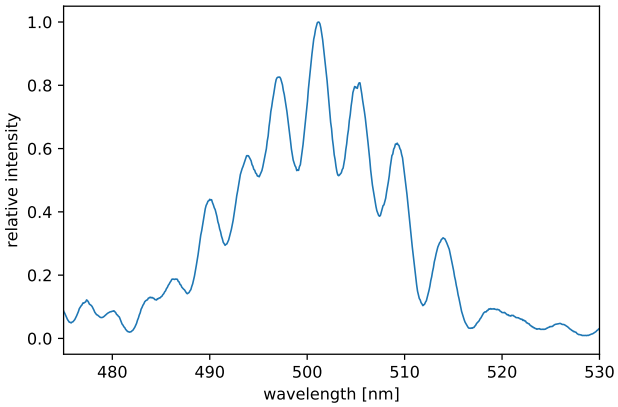

Figure 5: *A sample of how the interference pattern should look like. Out of the periodicity of the interference fringes, φ_{CE} can be calculated.*

The frequency doubled light can be described in a similar way as

$$E_{SHG}(\omega) = \gamma exp(2i\varphi_{CE}) \int \tilde{\varepsilon}(\omega - \omega_c)\varepsilon(\omega - \omega')d\omega' = \gamma exp(2i\varphi_{CE})\tilde{\varepsilon}^{SHG}(\omega - \omega_c), \tag{23}$$

and so the intensity is

$$\begin{aligned} I(\omega) \propto |E(\omega)|^2 =& |E_{fund}(\omega) + E_{SHG}(\omega)|^2 = |\tilde{\varepsilon}(\omega - \omega_c)| + \gamma^2|\tilde{\varepsilon}^{SHG}(\omega - \omega_c)| \\ &+ 2\gamma|\tilde{\varepsilon}(\omega - \omega_c)\tilde{\varepsilon}^{(SHG)}(\omega - \omega_c)|cos(\omega\Delta t + \varphi_{CE} + \frac{\pi}{2}). \end{aligned} \tag{24}$$

γ is a proportional factor including the second order susceptibility and a constant phase shift. Because E_{fund} and E_{SHG} are complex quantities, the $cos(x)$-term appears when calculating the intensity. Assuming that the amplitude of the pulses' envelope does not change on a shot to shot basis, the intensity for one specific ω does only depend on the CEP. It is not possible to directly read out the CEP of the spectrum, but by means of Fourier Transformation one can isolate the phase and thereby the CEP out of the $cos(x)$-term. The mathematical details on how to extract the phase are described in [9] and are not further discussed in this point.

1.3 High Harmonic Generation

The main principle behind the generation of attosecond pulses is the generation of so called high harmonics of a fundamental frequency. Harmonics are natural multiples of a certain frequency, in this case multiples of the carrier frequency of the incoming femtosecond infrared-pulse (IR-pulse). For light pulses, when multiples of the fundamental frequency of the electric field are created, the superposition of odd multiples results in even shorter pulses, while even ones cancel each other out. The whole process is of a quantum nature, so there are many quantum models to describe the generation of attosecond pulses, like the Lewenstein model or the time-dependent Schrödinger equation (TDSE). This short introduction will only focus on the Three Step Model, a semi-classical model that is very simple but yet describes most phenomena sufficiently accurate [10].

In the scope of this model, an atom is simplified as a nucleus that has a Coulomb potential and is surrounded by a bound electron, that is seen as a charged particle which has some quantum properties, for example it can tunnel out of a potential well, but also has classical properties like a mass m_e and a charge of e and moves according to classical mechanism [11]. The model describes three steps towards the generation of high harmonics: tunnel ionization, propagation and recombination [12].
In the first step, the electron leaves the potential of the core by tunnel ionisation. In the second one, it moves like a classical particle, accelerated by the electric field of the laser pulse. In the last step, the electron recombines with the ion and releases the energy gained by the acceleration of the laser pulse and the ionisation energy in form of a high energetic photon.
The more detailed version of the process is as follows:
The fundamental wave, in most cases an IR-pulse, strikes a noble gas atom. Normally, the electrons in the atom experience a coulomb potential resulting from the positively charged protons in the nucleus. But the incoming laser pulse has an electric potential as well and so the resulting potential changes in presence of a laser, because the potentials superimpose. Of course, the laser pulse only has a significant influence on the potential if the intensity is high enough, typically around $10^{14}\frac{W}{cm^2}$. This is shown in figure 6 on the top. As one can see, the potential has a finite threshold where the electron can tunnel out with a certain probability. The outcome of this step is a free electron and a positively charged noble gas ion.
The propagation of the electron in the laser-induced field is, like already mentioned, treated in a classical way in the framework of the Three Step Model. So by just applying Newtons equations of motion, one gets the electron's trajectory. Knowing the force (caused by the electric potential of the laser pulse), one can derive the acceleration and get the velocity as well as the position in dependence of the time at that the tunnel ionisation takes place by simple integration. An important factor is the so called ponderomotive potential

$$U_p = \frac{e^2 E_0^2}{4m\omega_0^2}, \tag{25}$$

that depends on the wavelength and on the intensity of the IR-pulse and is a measure for how much kinetic energy the electron gains in one circle of the electric field [13]. The trajectory depends highly on the point in time where the electron is released as shown in figure 6.
The last step is the recombination, where the electron returns to the ion and the kinetic energy as well as the ionisation energy are released in form of a high energetic photon. As this happens for every half cycle, an attosecond pulse train is generated, whose frequencies are odd integer multiples (only odd ones because of symmetry reasons, the even ones cancel each other out over one cycle) of the original frequency of the IR-pulse. The efficiency of the HHG is not quite good, because for many ionisation times the electron will not come back to the nucleus (see grey lines in figure 6).
The kinetic energy of the electron is proportional to the squared velocity of the electron and the time the tunnel ionisation takes place determines the velocity. The maximal energy of a photon can be $E_{max} = 3.17U_P + E_{ion}$. Emitted wavelengths are typically in a extreme ultraviolet (XUV) spectral range. The harmonic spectrum displays the intensities of each harmonic order, that directly corresponds to the wavelength and therefore to the energy of the released photon. It has a so called cutoff region near the frequency corresponding to E_{max}, the intensity of

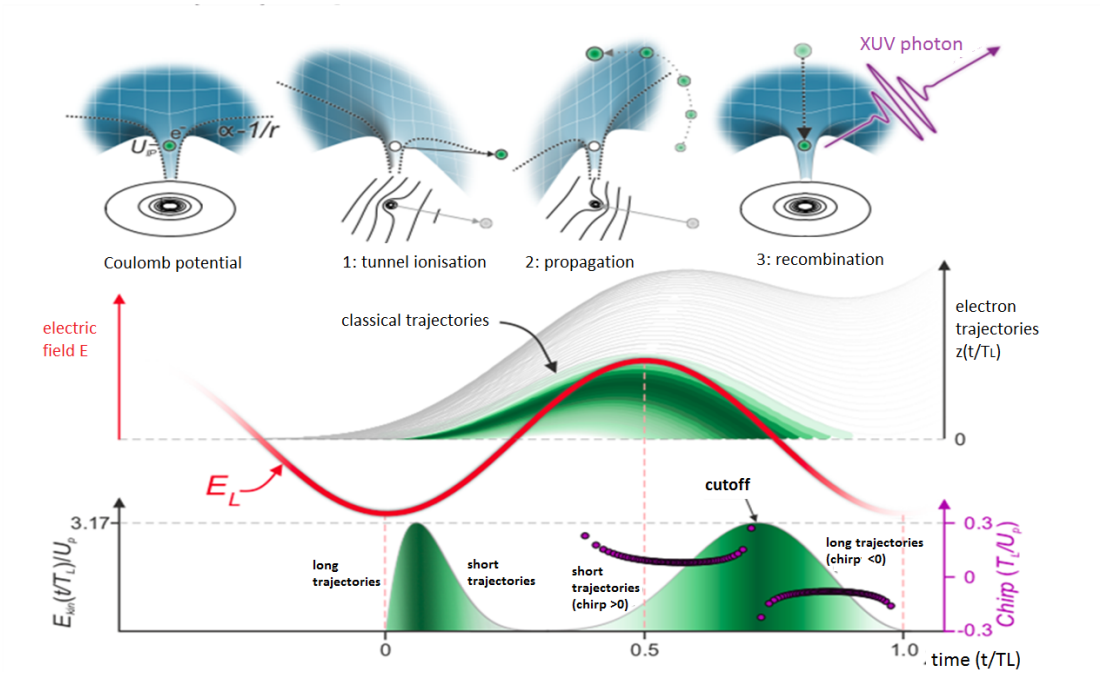

Figure 6: *Schematic illustration of the Three Step Model. The electron trajectories depend on the ionisation time and can be divided into "short" and "long" trajectories. There is only one ionisation time where the kinetic energy of the electron at the return time gets maximal. The harmonics emitted from this recombination process contribute to the cutoff in the harmonic spectrum. Taken from [13], modified.*

harmonics decreases strongly in that area. For a wide range of lower harmonic orders, there is a plateau region, where the intensity stays nearly constant over many harmonic orders [12].

2 Experimental Setup

The main purpose of the experimental setup in the Interatto laboratory at the Max Planck Institute for Nuclear Physics is to observe ultrafast quantum dynamics. As an instrument to do so, attosecond pulses are generated, which are on the same timescale as electrons move inside an atom. This opens new ways to do spectroscopy on a timescale that is, compared to one second, as long as one second is compared to the age of the universe [5].
By observing electron motion, new insights into the behaviour of quantum systems can be gained.
In this chapter, the general experimental setup of the laboratory is described with focus on the relevant details for CEP-stabilization. The femtosecond pulses are produced in a Ti:Sapphire amplifier system. Afterwards, the spectrum is broadened and the pulses are compressed so that they reach durations as low as a few femtoseconds. These pulses are used to generate even attosecond pulses by high harmonic generation that can be used for the previously mentioned spectroscopic experiments.

2.1 General setup

The femtosecond pulses are generated in a FEMTOPOWER^{TM}HE/HR CEP4 Ti:Sapphire multi-pass amplifier system, whose oscillator uses a titanium-doped sapphire crystal as a gain medium. This medium is pumped by a Spectra Physics Millenia pump laser at 3.5W [14].
Inside the mode-locked oscillator, there is a Piezo element that can be controlled by giving it a high voltage signal. The Piezo element consist of two glass prisms that can be moved and it is possible to steer the amount of glass inserted by the external high voltage signal. By this, the dispersion inside the oscillator can be changed. More details on the Piezo and its function can be found in chapter 3.2. The pulses are CEP stabilized right after they leave the oscillator by a FEMTOLASERS CEP4^{TM} module for FEMTOSOURCE^{TM}rainbow^{TM} that detects the CEO-frequency and substracts it from every comb line with a acousto-optic frequency shifter (AOFS). This is the so called fast loop CEP control, as it directly corrects the random phase shifts happening from pulse to pulse due to changes in the power of the pumping laser and changes of dispersion inside the resonator [15].
The corresponding slow loop is realized by the CEPset^{TM}, which was originally placed inside the amplifier but as part of this thesis was moved.
After leaving the amplifier, the laser beam enters a hollow-core fiber that can be filled with Helium. The index of refraction inside the Helium depends, if the intensity of the light is really high, on the wavelength of the light and gets non-linear [16]. So for high intensities like they are given in the experimental setup, self-phase-modulation takes place and this causes spectral broadening.
Two motorized wedges consisting of fused silica with an apex angle of 4° are installed after the fiber. By inserting or removing glass, the GDD of the pulses can be changed.
To counteract the dispersion happening in the hollow core fiber, and to also overcompensate the dispersion in the air, the beam is directed through a chirped mirror compressor. A chirped mirror induces a chirp on a pulse by delaying light with higher wavelengths more than lower ones ("negative chirp"), leading to anomalous chromatic dispersion and by this, to a compression of

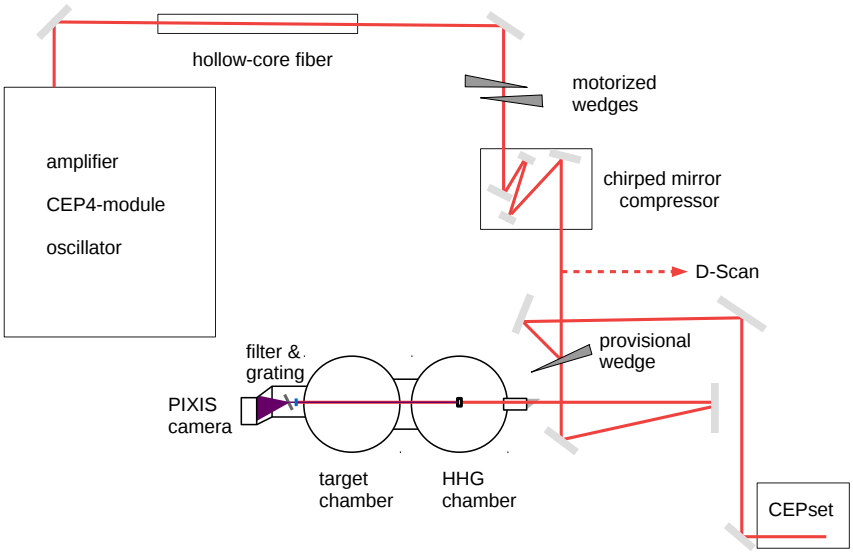

Figure 7: *The experimental setup. Schematic view, not to scale. The way of the IR-laser beam is represented in red, the one of the XUV-beam in purple.*

the pulse [17].

To determine the pulse duration, a dispersion scan (D-Scan) is implemented, where the second harmonic spectrum of the beam is detected in dependence of the thickness of the fused silica in the beam line. The amount of glass inserted is changed by moving the wedges and the resulting spectra are detected with a spectrometer. An iterative algorithm is used to produce a fit to the data. Out of this, it is possible to retrieve the phase and reconstruct the pulse, particularly the pulse duration [1].

Afterwards, the HHG takes place in an evacuated chamber. The theory behind High Harmonic Generation is described in chapter 1.3. In the chamber, noble gas streams out of a cell with an opening of $150\mu m$ and an interaction length of 3mm.

The beam is focused onto this cell by a focusing mirror outside of the chamber and enters the chamber through a window of fused silica, which is placed in the Brewster angle to maximize the amount of light transmitted.

Finally, the pulses enter the target chamber, which is evacuated, too, like the whole beam path after the entrance window. Otherwise, the pulses would interact with the air and could not propagate . In this chamber, it is possible to do spectroscopic experiments by letting gas stream in and observing the atoms or molecules with the ultrashort pulses. This procedure is of minor interest for this thesis, so it will not be described in detail.

After the HHG, the original IR-pulse propagates along with the additional, newly generated attosecond pulse train. There are different filters mounted to select only the attosecond pulses and get rid of the fundamental IR-pulse. Afterwards, a grating is installed in order to separate the different wavelengths and therefore energies of the incoming light. Finally, the harmonic spectrum is detected by a Princeton Instruments PIXIS XUV-camera.

2.2 Setup of the f-2f-interferometer

The CEPset^{TM} module was set up next to the HHG chamber, so that the CEP can be measured and controlled precisely right where CEP stability is most important. It was intended to use the light that is reflected from the entrance window for measurements, because in this case the implementation of the CEPset^{TM} interferometer would not affect the beamline at all and it would make use of the last opportunity to detect the CEP before the beam enters the attosecond beamline. It was recognized that the power from the reflex was not enough to generate second harmonics in the BBO crystal. So for all the experiments done in this thesis, a wedge consisting of fused silica was put in the path of the beam shortly before the focusing mirror directs the light into the HHG chamber (see figure 7). With this reflex, a much higher intensity than the one from the entrance window could be achieved, because the angle of the wedge and therefore the reflectivity could be chosen without restrictions. The entrance window into the HHG chamber was designed specifically for as little reflection as possible, because it is intended to have high intensity for the experiments. It should maximize the transition of the (almost completely p-polarized) light and therefore the Brewster Angle was chosen as the angle between window and beam.

By using the wedge, there is additional glass in the beamline that influences the properties of the pulse by causing an additional chirp. To make the wedge unnecessary, which is important for further experiments, a new angle for the entrance window was calculated. This way, enough light should be transmitted into the chamber to do experiments where high intensity is required, but there should still be enough power for SHG in the f-2f-interferometer delivered.

For the following calculations, first, the polarization of the light right before the entrance window was measured with a polarization filter and a power meter. It was confirmed that the light was almost completely p-polarized by finding a minimal power slightly higher than the background power detected without any beam at all when setting the polarization filter vertically. The full, unattenuated beam had a power of around 2.3W right before the HHG-chamber. This value depends on the parameters of the hollow-core fiber and on the beam alignment, so the power changes slightly from experiment to experiment. Therefore, this is not an exact calculation but more a rough estimation to decide what angle will deliver sufficient power for the f-2f-interferometer.

As experiments showed, an intensity of about 40mW is required right before the beam enters the CEPset^{TM}, this implies that the reflectance should be around 2%. The reflectance can be derived by using the Fresnel equations [18], which describe the amount of light that is reflected and transmitted when changing the medium it is going through, and Snells law (equation 27), which tells about the change of the angle of the light when entering a different medium [18]:

$$R_p = \left(\frac{E_{0r}}{E_{0e}}\right)^2 = \left(\frac{n_2 cos\alpha - n_1 cos\beta}{n_2 cos\alpha + n_1 cos\beta}\right)^2 \tag{26}$$

$$n_1 sin(\alpha) = n_2 sin(\beta). \tag{27}$$

R_p is the reflectance for p-polarized light and n_i is the index of refraction of each medium. The meaning of the angles can be seen in figure 8.

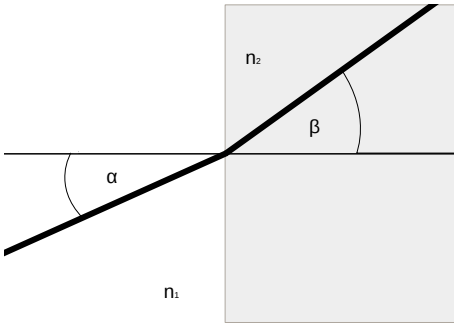

Figure 8: *Definition of the angles in this chapter*

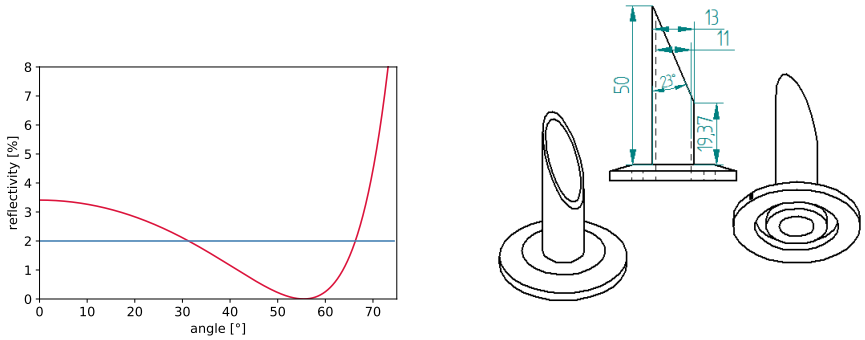

Figure 9: *left: graphic illustration of equation 28. The reflectivity of p-polarized light is plotted in dependence of the angle of the incoming light as defined in figure 8. The angle where the reflectivity vanishes is the Brewster Angle. As a reflectivity of* 2% *is desired, a line at that value was plotted, too. right: the new entrance window with an angle of* 67°

The index of refraction of air is $n_1 \approx 1$. The one of fused silica does not only depend on the temperature, but also on the wavelength. It is for wavelengths in a range between 210 nm and 3710 nm and at standard conditions described by the Sellmeier equation [19]. Inserting the central wavelength of the pulse at the position of the entrance window (which is around 790nm) delivers $n_2 = 1.453$. The only free parameter now is the angle between the entrance window and the beam. A power of slightly more than 40mW, corresponding to 2% of the total beam power, is desired. The following equation can be derived out of equations 26 and 27 by using basic trigonometric relations:

$$R_p = r_p^2 = \left(\frac{\tilde{n}^2 cos(\theta) - \sqrt{\tilde{n}^2 - sin^2(\theta)}}{\tilde{n}^2 cos(\theta) + \sqrt{\tilde{n}^2 - sin^2(\theta)}} \right)^2 . \tag{28}$$

This function, where $\tilde{n} = \frac{n_2}{n_1}$ is plotted in figure 9. There are two solutions for $R = 0.02$, which were found numerically by using Wolfram Alpha to be $\theta = 66.3°$ and $\theta = 31.3°$.
To avoid a realignment of mirrors in the experimental setup, the angle of $\theta = 67°$ was chosen for the new entrance window.
The current one with the Brewster Angle of 55.5° will soon be replaced by the new one. A sketch of the new aperture, done with Solid Edge, can be found in figure 9 and an additional technical sketch is in the appendix (23). This new entrance aperture will be produced and set

up in the laboratory setup afterwards, but as the production takes to long, implementation and testing of the new window will not be part of this thesis anymore.

3 Controlling the CEP

After a short general introduction into the theory of control loops, the implementation of the CEP-stabilization is explained. Properties of this control loop have been observed and long term measurements with and without enabled control loop are evaluated to characterize the system.

3.1 A short introduction to control engineering

Control loops are important in a scientific and engineering context. The main idea behind a control loop is that the current value is measured and compared to some desired value. Therefore, systems can be stabilized and their behaviour can be fixed. An example for such a system is shown in figure 10. In contrast to open-loop control systems, closed-loop control systems provide a feedback on how the output of the system is behaving in comparison to the desired output response [20].

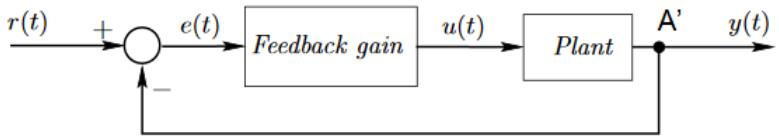

Figure 10: *The basic scheme of a closed loop feedback system. Taken from [20], page 35.*

As one can see in figure 10, a signal is detected and compared to the desired value. The difference e(t) between those is gained as a feedback and by a function u(t), whose properties depend on the exact loop, the plant calculates a control value. The new signal is measured and given back to determine a new difference value e(t).
An often used control mechanism is a P(roportional)-I(ntegral)-controller. There are two control terms, one that is proportional to the deviation e from the desired value (P-term u_p) and one that integrates the deviation over time (I-term u_i) [20]:

$$u_p = K_p e \tag{29}$$

$$u_i = K_i \int_0^t e(\tau) d\tau. \tag{30}$$

The constants K_p and K_i are the parameters that characterize the system. A pure P-controller, where $K_i = 0$, reacts really fast, but it cannot reach the exact desired value and there is a permanent deviation. This is why the I-term is added: it integrates over the deviation and therefore increases the precision and the long term stability.

3.2 Description of the control loop

The phase control loop of the CEPset^{TM} is implemented as follows: The intensity spectrum is detected by the spectrometer and can be read out by a computer. The FEMTOLASERS$^{\text{TM}}$ CEPset^{TM}-software calculates the CEP (for details on the detection, consult chapter 1) and

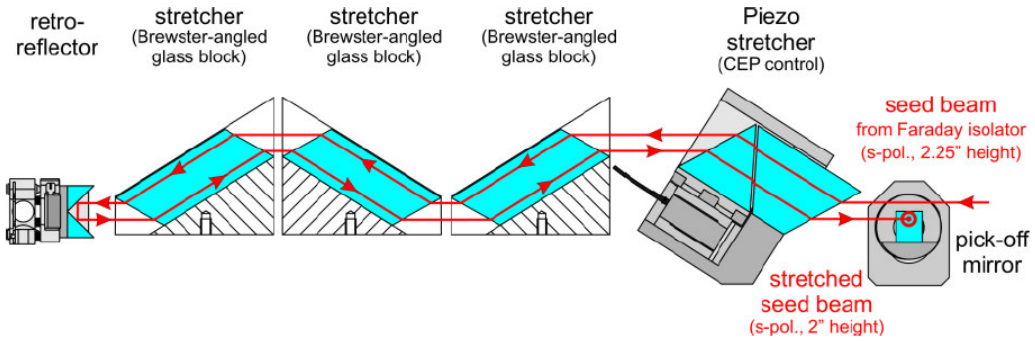

Figure 11: *The Piezo Stretcher Actuator inside the oscillator. Picture taken from [21]*

compares it to a desired value that the user can define. A control value is generated by the software to counteract the change. The CEPset^{TM} has an electronics unit, where a 16-bit digital-to-analog-converter (DAC) converts this control value into an electronic signal for the Piezo Stretcher Actuator, which is amplified by the Piezo Stretcher control into a high voltage signal.

The Piezo Stretcher Actuator consists of two glass prisms (see section 11). One of these is fixed and the other one can be moved in respect to the fixed prim. The movement depends on the given signal, therefore the amount of glass insertion can be changed and the CEP can be kept constant without changing any other beam parameter or the beam pointing [8]. The CEP can be regulated by changing the amount of glass, because the index of refraction of glass is higher than the one of air. So the phase shift Ψ (compare to equation 8) gets higher with the amount of inserted glass, as the length L of the beams path through that medium increases.

In the CEPset^{TM}-software, the user can define the parameters K_p and K_i of the control loop manually. Values from 0 to 999.9 can be chosen for both, with a stepwidth of 0.1.

The spectrometer inside the f-2f-interferometer is triggered by a TTL trigger signal that is produced by the electronics unit in order to synchronise the spectrometer to the laser repetition rate, so that only one pulse is detected at a time. The integration time of the spectrometer of course has to be short enough that pulses can be detected on a shot to shot basis (around 330 μs for the used Ti:Sapphire laser, which has a repetition rate of 3 kHz). The trigger divider can be set to an arbitrary natural value between 1 and 128. The meaning of this value is on what basis the measurement takes place; for a value of n, only every nth pulse is taken into account for CEP measurements.

It is important to emphasize again that the pulses already are CEP stabilized after the oscillator. So the purpose of the control loop is not to stabilize the phase in first place, as the changes happening inside the cavity are regulated by the CEP4-module as described in section 2. It is to compensate phase drifts occurring inside the amplifier and while the beam propagates towards the attosecond beamline. These appear mainly because of air flows, fluctuations in temperature and dust. This is the reason why the interferometer was moved out of the amplifier, where it was placed before: if the CEP is kept constant before leaving the amplifier, the carrier-envelope phase at the HHG-chamber is not necessarily constant anymore as there is no opportunity to

take countermeasures against these drifts that are happening while the pulse propagates.
To quantify changes in the CEP over a longer period of time, a long term measurement of the CEP without stabilization was done.

3.3 Long term measurement without control

The purpose of the experiment was to quantify the naturally occuring changes in the CEP after the fast loop stabilization. The CEPset^{TM}-module was set up like described in section 2.2, but the CEP control loop was disabled.
The f-2f-interferometer detected the interference pattern of the fundamental beam and the second harmonic beam and the CEPset^{TM}-software calculated the corresponding CEP. As already mentioned in the chapter about the theoretical background, the CEP is always measured modulo 2π. But for more clearness, in this chapter the phase is treated as continuous. Also, one has to keep in mind that only a relative measurement of the CEP is possible, so an arbitrary offset can be added to all values.
In the following chapters, there were measurements done with two slightly different configurations:
for both of them, the experimental setup is built up like described in section 2, but the first one does not have any helium inside the hollow-core fiber, while the second one does.
The effects of not having helium in fiber are the following:
First of all, the spectrum looks different (see figure 12). Without helium, self-phase-modulation does not take place because the index of refraction stays constant and is equal for all wavelengths and as a result of this, the spectrum is not broadened. Second, the pulse is longer than if it would have passed the fiber filled with helium. This is a direct consequence of the narrow spectrum, because the spectral components and the pulse duration are connected over a Fourier-transform, and a broader spectrum therefore leads to shorter pulses (frequency-time-uncertainty). For longer pulses, changes in the CEP are less significant for the pulse shape (see figure 3). There are two different reasons for doing two measurement series: First, there was the guess that the helium could cause changes in the spectrum of the laser pulses that are not correlated to the CEP, but change the interference pattern inside the f-2f-interferometer. So an apparent change in the CEP would be detected and regulated against, but in reality, this would not have the desired stabilization effect, as the pattern would not represent the wanted signal. This is examined in section 3.6.
Second, to have a reference measurement with longer pulses which the actually relevant values (the ones gotten with helium inside the fiber, like it is the case for every standard experiment) can be compared to.
The long term measurements are shown in figure 24. The phase is, like already mentioned, plotted without caring about the 2π-periodicity to illustrate the phase drifts better. A more detailed diagram of the phase drifts can be found in the appendix in figure 24 and 25.
For longer pulses, one can see that there are enormous drifts of the CEP. There are periods of some seconds where the changes are happening slowly with few mrad per second, but there are also oscillations where the CEP changes rapidly, these happen on a shorter time scale of less than a second.

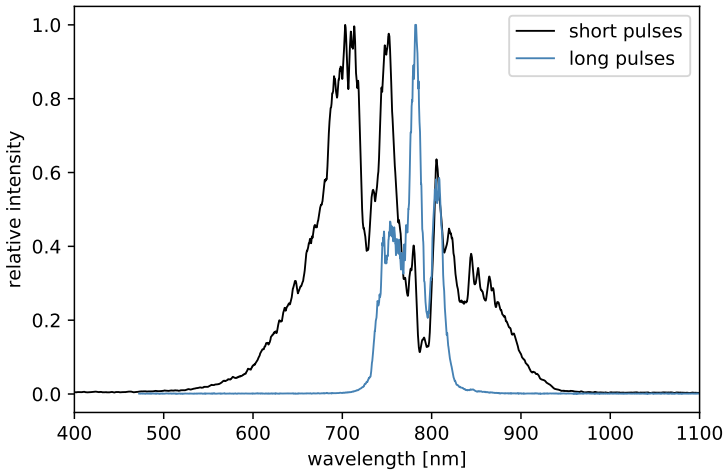

Figure 12: *The spectra of the pulses with helium inside the hollow-core fiber ("short pulses") and without("long pulses").*

Reasons for the changes in the CEP are changes in the medium the light is propagation through, especially in the air, like streams, local temperature differences, dust particles etc.
Over the whole process, there is always some jitter in the range of some mrad. These are statistical fluctuations that always appear and that, as one will see later, can not be regulated out.
The CEP is a lot more stable for shorter pulses. The long term drifts are smaller and also the jitter is less.

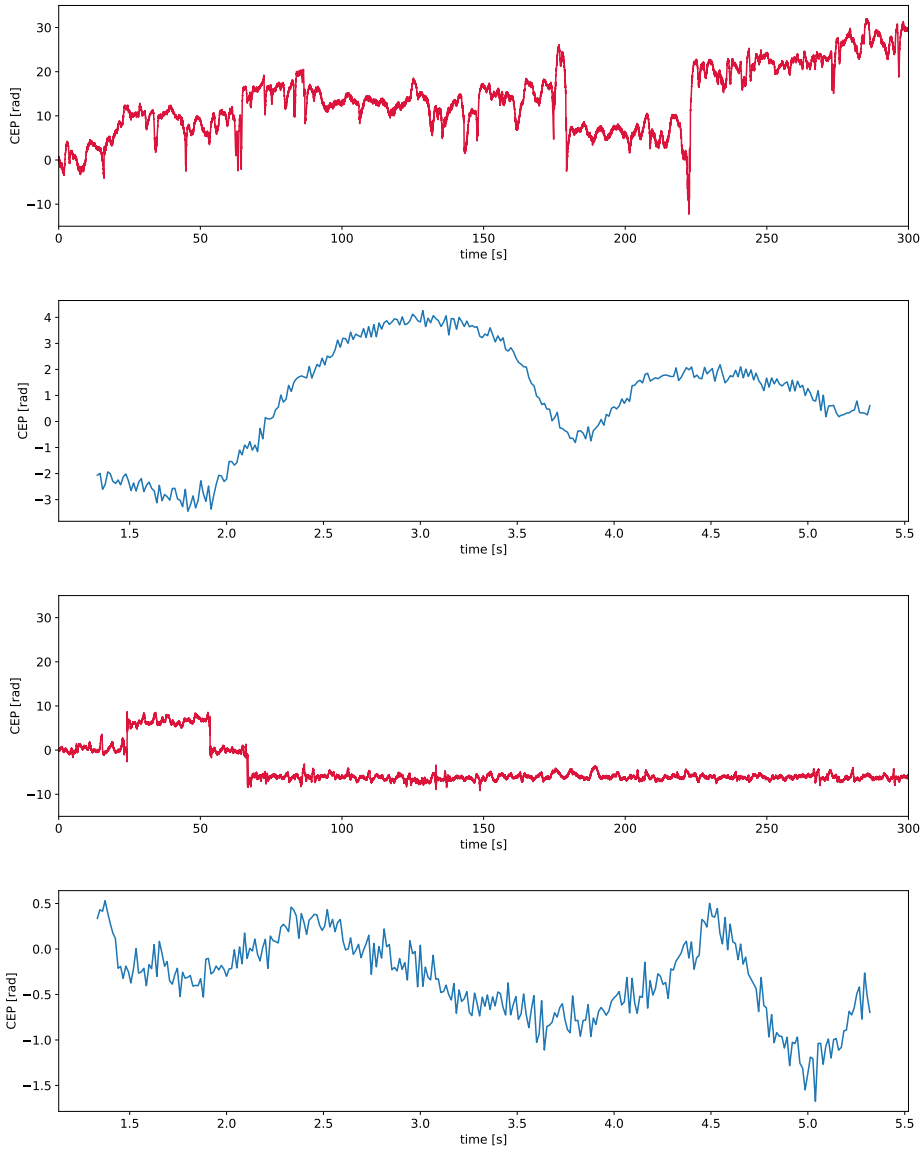

Figure 13: *Long term measurement of the CEP without stabilization. The first diagram is an overview of the CEP over the whole period of measurement for long pulses, in the second diagram a shorter period of time is represented, so that the short term jitter of the CEP is visible. The same holds for diagram 3 and 4, where short pulses are observed.*

3.4 Characterization of the system

To understand the control loop better, an attempt was made to quantize the system. One point of interest was how applying a specific DAC-control-value corresponds to a change in CEP. For this, there were some measurements done in which a linear change of the DAC-control values was applied. Sweeping the control value from the lowest one (-2^{15}) to the highest one (2^{15}) in a constant speed leads to constant changes in CEP (see figure 14). By getting the change of the DAC with time and the change of the CEP with time, one can derive

$$\frac{\Delta CEP}{\Delta DAC} = \frac{\Delta CEP}{\Delta t}\left(\frac{\Delta DAC}{\Delta t}\right)^{-1}. \tag{31}$$

There was a linear fit applied throughout the measured CEP and DAC values to get $\frac{\Delta CEP}{\Delta t}$ as well as $\frac{\Delta DAC}{\Delta t}$ like shown in figure 14.

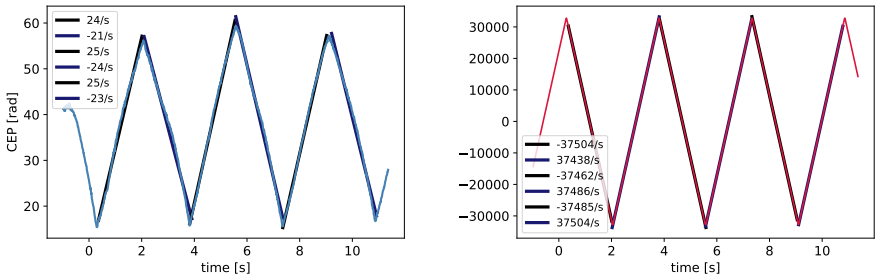

Figure 14: *Quantification of the change of the CEP with the DAC control value. CEP and DAC control value were measured simultaneously. The parameters in the legend are the slopes of the fitted black and blue curves. The errors are estimated out of the standard deviation of the slopes for ascending and descending values.*

By applying equation 31, one gets a change of the CEP with the DAC control values of (66.9 ± 2) mrad/DAC for ascending DAC-values and (62.2 ± 4) mrad/DAC for descending DAC-values. As a benefit, by testing the change of the CEP in dependence of the inserted glass it can be shown that the interference fringes detected by the interferometer are actually the desired signal for determination of the CEP and do not have another origin, like for example interference of the fundamental beam with a reflex of itself. For a reflex or any other kind of false interference signal, the signal would not be sensitive to a change of first-order-dispersion done by the Piezo and would not change linearly with the DAC value.

3.5 Finding suitable control parameters

For an optimal control, it is necessary to find the right set of parameters K_p and K_i (see equation 29 and 29). "Optimal control" means in this context that the system reaches the desired value of the CEP again as fast as possible whenever fluctuations appear and that there are no overshoots or oscillations. You can find some exemplary parameters and the corresponding behaviour of the system in figure 16.
As the CEP is changing constantly and in a random way, it turned out not to be not possible to apply a standard procedure on how to get the optimal parameters.

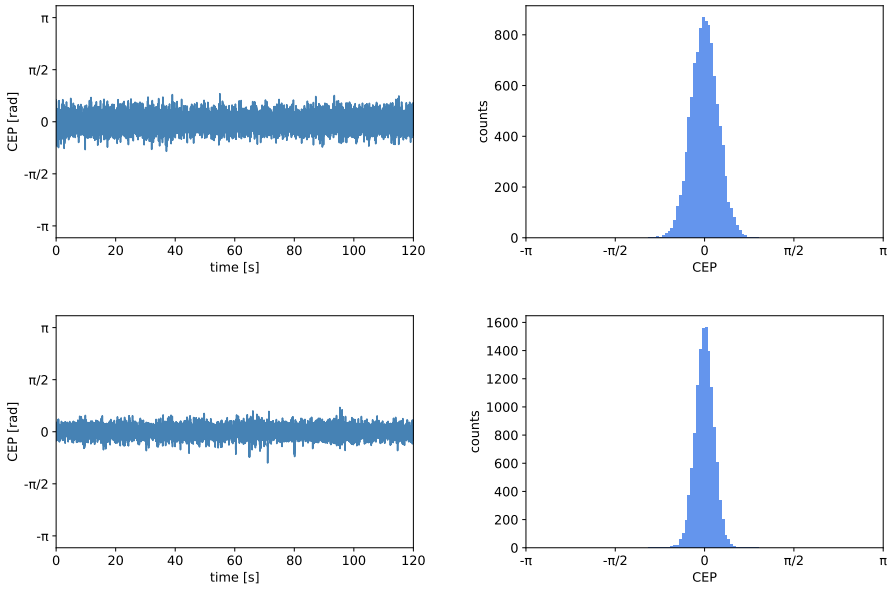

Figure 15: *Long term measurement stabilized without (top) and with (bottom) helium inside the hollow-core fiber. Target CEP is 0 rad, the actual mean is 0 rad with a standard deviation of 236 mrad in the first case and 163 mrad in the second case.*

So a heuristic technique was chosen to determine satisfying parameters. The advantage of this method is that there are no requirements on the reaction of the system to changes. Just by observing the system, especially the standard deviation of the desired value for different control values, a good set of parameters can be found. The disadvantage is that maybe not the globally optimal values are chosen, but only a local minimum of deviation has been found.
By using this method, sufficiently accurate parameters have found to be $K_p = 10$, $K_i = 900$ for the current experimental setup, for the measurements with helium in the fiber as well as for the ones without.
A long term measurement with applied control loop for both cases is plotted in figure 15.
It is possible to get a mean CEP of 0 rad even over a longer time. The standard deviation in the case of the fiber filled with helium is with 236 mrad higher than for short pulses, where the deviation is only 163 mrad.
After doing the long term measurement without control, this is not a surprising fact, because even without applied control loop, there were less and slower changes in the CEP for short pulses.

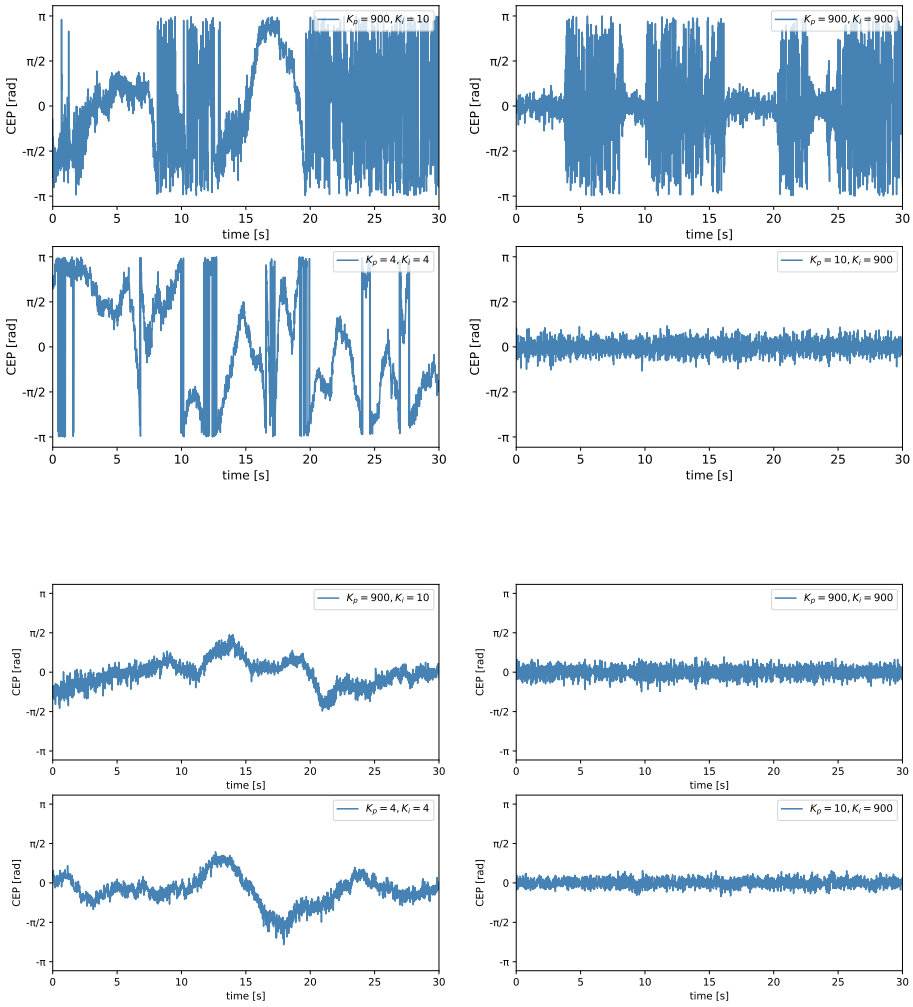

Figure 16: *The first four diagrams show the CEP over time for different control values for long pulses. The second collection of four diagrams compares different parameters for short pulses.*

3.6 Spectral changes and CEP

To explain that is done in the next chapter, equation 24, which is the key for determination of the CEP out of the intensity pattern, is repeated first:

$$I(\omega) \propto |\tilde{\varepsilon}(\omega-\omega_c)| + \gamma^2 |\tilde{\varepsilon}^{SHG}(\omega-\omega_c)| + 2\gamma |\tilde{\varepsilon}(\omega-\omega_c)\tilde{\varepsilon}^{SHG}(\omega-\omega_c)| cos(\omega\Delta t + \varphi_{CE} + \frac{\pi}{2}) .$$

As already mentioned in chapter 1.2.3, it is possible to extract the phase out of the intensity pattern by doing a Fourier transformation. But this only holds if neither the fundamental spectrum $\tilde{\varepsilon}(\omega-\omega_c)$ nor the second harmonic spectrum $\tilde{\varepsilon}^{SHG}(\omega-\omega_c)$ changes in time. The form of $\tilde{\varepsilon}^{SHG}(\omega-\omega_c)$ is only dependent on $\tilde{\varepsilon}(\omega-\omega_c)$ during the measurements. Any factors that influence the shape of the SHG-spectrum independently from the fundamental spectrum, like the angle of the BBO crystal or the rotation of the PBS, are not changed during the measurement process.

So it was checked if the fundamental spectrum itself is constant over time. To do so, a fiber spectrometer was set up to detect the fundamental spectrum right after passing the wedge in front of the HHG-chamber. The detection happened by blocking the beam with a beam blocker and orienting the spectrometer towards the blocked beam to detect the stray light, so that the interferometer does not oversaturate. The reflex intended for CEP-stabilization was not affected by that, so stabilization of the CEP was still possible during the measurements.

How the spectra with and without self-phase-modulation look like in general has already been illustrated in figure 12.

In the following, the spectra are shown in dependence of time (figure 17). The integration time was 100 ms for each spectrum and the recording was continuous.

The standard deviation for each wavelength has been normalized with respect to the mean spectrum over the measured time. There is no significant difference between the changes in the spectrum with or without activated CEP control.

Out of the plots is is noticeable that the standard deviation varies a lot along the wavelength-axis and is higher especially in the areas where the intensity of the laser is low. This might be, because the count rate is much lower for these areas and therefore statistical influences play a greater role.

The wavelengths relevant for detection of the CEP are the ones around 900 nm and 450 nm, as the fundamental light at wavelengths of slightly more than 450 nm interferes with the frequency-doubled light originating from around 900 nm. The spectra in figure 17 have been obtained without an additional sapphire plate, which broadens the spectrum even more. The sapphire plate does not only broaden the spectrum, it is another source of fluctuations in intensity itself. It is clearly visible even by eye that it induces additional temporal changes in the spectrum, because the intensities for different wavelengths vary a lot right after the plate.

The fluctuation of the lower (less than 650 nm) as well as of the higher wavelengths (more than 900 nm) is much higher for the spectra recorded without helium inside the hollow-core fiber. This might explain, why even the stabilized CEP varies more for longer pulses than for short pulses: the signal that is detected fluctuates uncontrollably with the spectrum and this

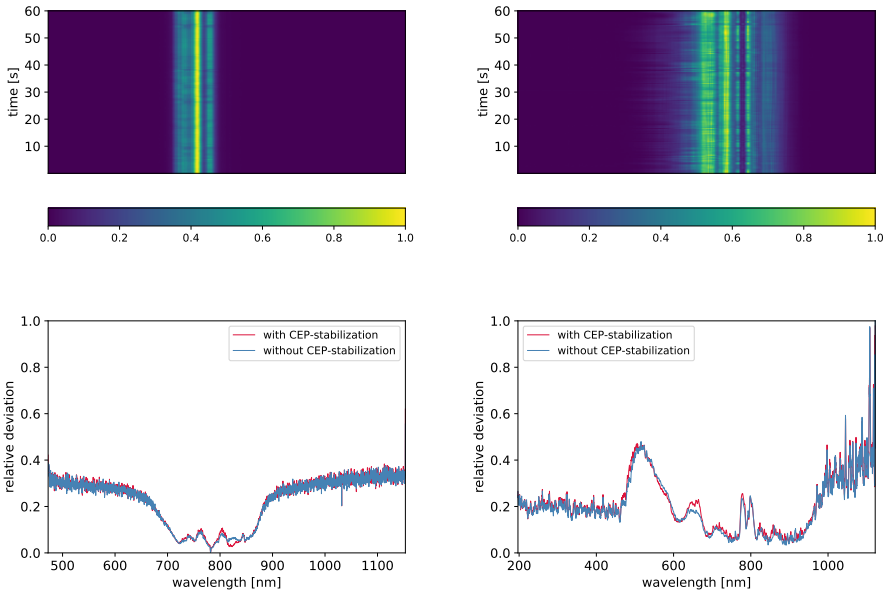

Figure 17: *Spectra with applied CEP-control for long (left) and for short (right) pulses over time. The standard deviation for each wavelength over the whole measurement period is shown as a fraction of the mean intensity at that specific wavelength and is illustrated in the lower plots. Spectra without CEP-control have been recorded, too. The plots are aligned in a way that the wavelength scale applies for both, the deviation and the spectrum itself.*

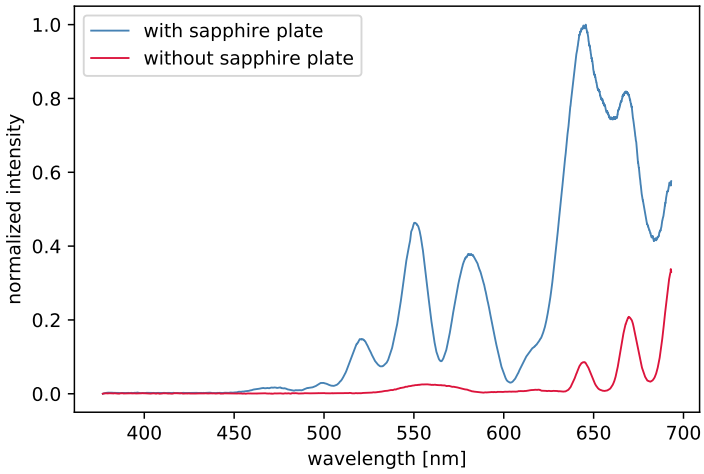

Figure 18: *Spectral broadening by the sapphire plate. The blue spectrum was obtained by the Ocean Optics Flame spectrometer inside the CEPset^{TM} after optimizing the white light generation at the sapphire plate and with removed BBO crystal. After removing the sapphire plate and with an otherwise unchanged setup, the red spectrum was recorded. This analysis was only done for short pulses.*

affects the performance of the control loop negatively. So, in contrast to the expectations, the regulation of CEP while having helium inside the fiber is more effective than the other way around.

4 CEP-dependent measurements on High Harmonics

The CEP influences the harmonic spectrum in a known way [22] [23] [24] [25]. So the main reason for doing the CEP-dependent measurement of the harmonic spectrum is that High Harmonic Generation is an established method to show if controlling the CEP with the previously described setup is actually possible. That is, because some of the changes in the harmonic spectrum with CEP are known. So if changing the desired value of the CEP in the control loop changes the harmonic spectrum in the expected way, the CEP can indeed be controlled in a way that is useful for future experiments.

4.1 Expected effects of the CEP on the harmonic spectrum

Two aspects of the dependence of the harmonic spectrum on the CEP are investigated as a part of this thesis:
First, there is an energy shift of the harmonics in the cutoff region expected if φ_{CE} is changed. Second, the intensity of these harmonics should depend on the CEP.
The so called strong field approximation (SFA) predicts that for harmonics in the plateau region of the harmonic spectrum, there are two quantum paths, that are associated to the two classical electron trajectories (long and short trajectory, see figure 6) that contribute mainly to the dipole moment [23]. It can be selected if long or a short quantum paths should be dominant in HHG by moving the position of the cell in respect to the focus: if the gas jet is located after the focus, the amount of short paths increases and if it is placed before the laser focus, the number of long paths increases [22]. This is because moving the gas jet changes the phase matching.

For few-cycle laser pulses, only up to two photon emissions that contribute to the cutoff region are possible for each pulse. The phases Φ_1 and Φ_2 are associated with these emissions. Every phase is given by [23]

$$\Phi = \omega t_r - \frac{1}{\hbar} S(p, t_0, t_r), \tag{32}$$

where $S(p, t_0, t_r)$ is the semi-classical action along the considered stationary action trajectory that depends on the momentum p of the electron and on the times of ionisation t_0 and return t_r. ω is the frequency of the emitted light.

$$\Delta\Phi = \Phi_2 - \Phi_1 \tag{33}$$

is now the phase difference of the two quantum pathways. This phase difference, as explicit calculations of $\Delta\Phi$ done for short trajectories in [23] show, depends linearly on the frequency ω of the emitted photon and therefore on the harmonic order. Also, there is an additional dependence on the CEP. This dependence is not obvious from the given formula but follows by explicitly calculating the semi-classical action mentioned above for laser pulses with different CEP which is not reproduced here.
So a different φ_{CE} leads to a different phase shift, like shown in figure 19. That induces a shift in position for different CEPs.

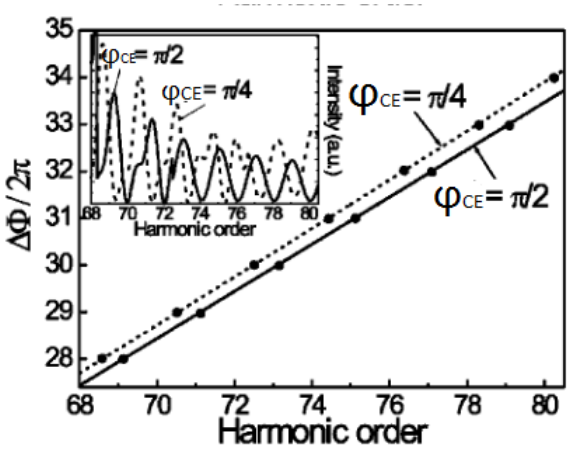

Figure 19: $\Delta\Phi$ *depends linearly on the frequency* ω *of the harmonic radiation . Also,* Φ *changes with* φ_{CE} *as explicit calculations of the electron dynamics in the IR-field of the laser show. Taken from [22], modified.*

The change of intensity can be explained completely by means of the Three Step Model: For $\varphi_{CE} = 0$ the maximum kinetic energy of the recombining electron is higher than for other CEPs, where the peak intensity and the ponderomotive potential is lower [25]. So there is a higher yield of photons with cutoff energy for $\varphi_{CE} = 0$ and therefore the detected intensity increases.
For really short few-cycle pulses, like the upper ones shown in figure 3, the last peak in the cutoff could even disappear for some CEPs because it would not be possible for the electron to gain enough energy [25]. For longer pulses, the difference is not that high, so that peaks mostly do not disappear, but the intensity changes nevertheless.

4.2 Experimental details

The general experimental setup was already described in section 2. Unlike in the chapter before, only measurements with helium inside the hollow core fiber were done. A pulse duration of (6.5 ± 0.2) fs was determined by a D-Scan.
Inside the HHG-chamber, High Harmonics were generated in argon with a backing pressure of 115 mbar. By moving the wedges in front of the chirped mirrors (see chapter 2), the dispersion of the pulses was optimized. Also, the cell inside the HHG-chamber was located after the focus, so the short paths are the preferred electron trajectories. This is an important detail, because the derivation described in the last section was done for short electron paths only.
The CEP was selected from -2.2 rad to 2.2 rad in steps of 0.2 rad so any periodicity equal or less than π should be visible. The chosen value was set in the CEPset^{TM}-software.
The control parameters found in chapter 3.2 were used for CEP-stabilization. The standard deviation of the CEP was determined to be 163 mrad again.
A desired value of φ_{CE} was chosen in the CEPset^{TM}-software and the harmonic spectrum was detected by the PIXIS XUV-camera 10 times per CEP with an integration time of 100 ms in each case. The PIXIS camera has 1340 pixel in horizontal direction, representing the energy.

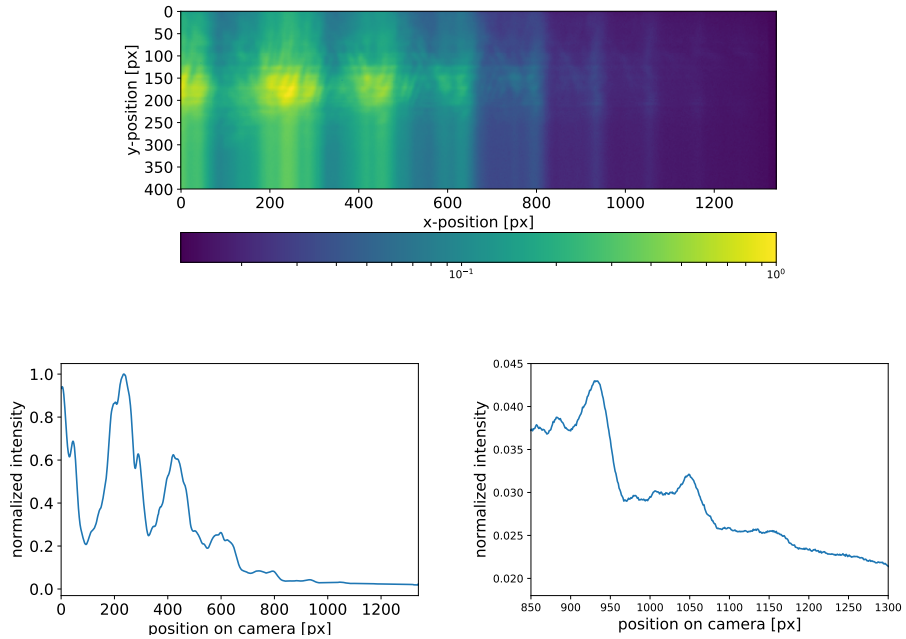

Figure 20: *In the upper image, the normalized intensities detected in each pixel of the camera are plotted logarithmically, so that the peaks in the cutoff region, those intensity is much lower than the one of peaks in the plateau region, are visible. Out of this, the spectrum in the second diagram was extracted by integrating the intensities from the* 120^{th} *to the* 190^{th} *vertical pixel. The lower right plot shows the cutoff region in detail. These peaks that are the ones of main interest in this chapter. For simplicity, the peak at about 920 pixel will be referred to as "left" peak and the one at around 1150 pixel as "right" peak.*

Knowing the exact energy of the Harmonics is not needed for this qualitative evaluation, so no energy calibration was done. However, it is important to note that the dependency of energy and pixel is not a linear one and that the energy increases for higher pixel positions. The position of the camera can be changed to look at different regions of interest in the harmonic spectrum. For the following experiments, only the cutoff region is important, so pictures of this area were taken. One sample image taken by the camera is displayed in figure 20.

4.3 Experimental results

Out of the detected images, one can derive an intensity spectrum like described in figure 20. To get the position of the harmonic peaks, for every single spectrum the harmonic intensity was plotted and a gaussian function including an offset and an additional linear term to correct for the background was fitted to the last three peaks visible in the cutoff region and also to the one in the plateau region that is located approximately at pixel 220:

$$y = Aexp(-\frac{(x-\mu)^2}{2\sigma^2}) + bx + c. \tag{34}$$

By applying fits like this, the position μ and the intensity A for each peak are determined.

The positions of these peaks are plotted in dependence of the CEP in figure 21. There is one grey point for each measurement and the red points are the mean positions for each CEP. The error of the mean peak position was determined by calculating the standard deviation out of the individual positions.
For each peak, a periodicity in the position with respect to the CEP can be seen. A linear fit,

$$y = ax + b, \tag{35}$$

was applied to each part. Theoretically, the shift is expected to be linear in the frequency. As the energy does not depend on the pixel linearly, the shift in the peak position on the camera does not necessarily need to be linear. But as only small changes of the position of few pixel occur, it can be estimated as linear.
The resulting slopes of the fits are shown in the following table, where Δ a is the error of the slope resulting of the fit. The parameter a is for CEPs less than $\varphi = 0$ and a' for the positive ones.

approximate peak position [px]	a [px/CEP]	Δ a [px/CEP]	a' [px/CEP]	Δ a' [px/CEP]
930	-4.5	2.4	-3.8	2.35
1050	-2.0	1.5	-2.6	1.5
1150	-6.6	3.2	-8.0	3.35
230	0.1	2.5	-1.5	2.15

Table 1: *The shift of the harmonic orders with CEP.*

That the jump in the position appears for every harmonic at the same CEP indicates that the observed effects are actually due to the changes in φ_{CE} and not just coincidence. Additionally, the slopes of the lines agree within the error limits for every peak and differ significantly from zero for the peaks in the cutoff. The peak in the plateau whereas does not shift, which is also one of the expected results.
The relative errors are enormous and as such, this analysis can not be the basis of a quantitative evaluation of the influence of the CEP on the harmonic spectrum. Qualitatively, the shift of the harmonics is clearly visible. But in general, there are to many sources of error to obtain reliable results out of the data. Not only the non-linearity between energy and number of pixel is a problem, but also the huge fluctuations of the position for a single CEP, that can be seen in the plots where the individual measurements are illustrated (figure 21). To really determine if the occurring pattern is significant, further observations are needed.
Not only the peak positions, but also the intensities were determined. They are depicted relative to the intensity at $\varphi_{CE} = 0$ in figure 22. Like for the positions, every single intensity was determined and afterwards, the mean value and its error were derived.
Looking at the intensity, a periodic structure should be noticeable in theory, too. But as the plots show, there is no such structure visible. The standard deviations of all relative intensities is shown in table 2.
The intensity in the plateau region changes as much as for the peaks in the cutoff, even though it should not change at all according to the theory. So the experiment seems not to be sensitive enough to intensity changes to detect the expected intensity modulation. The high fluctuations

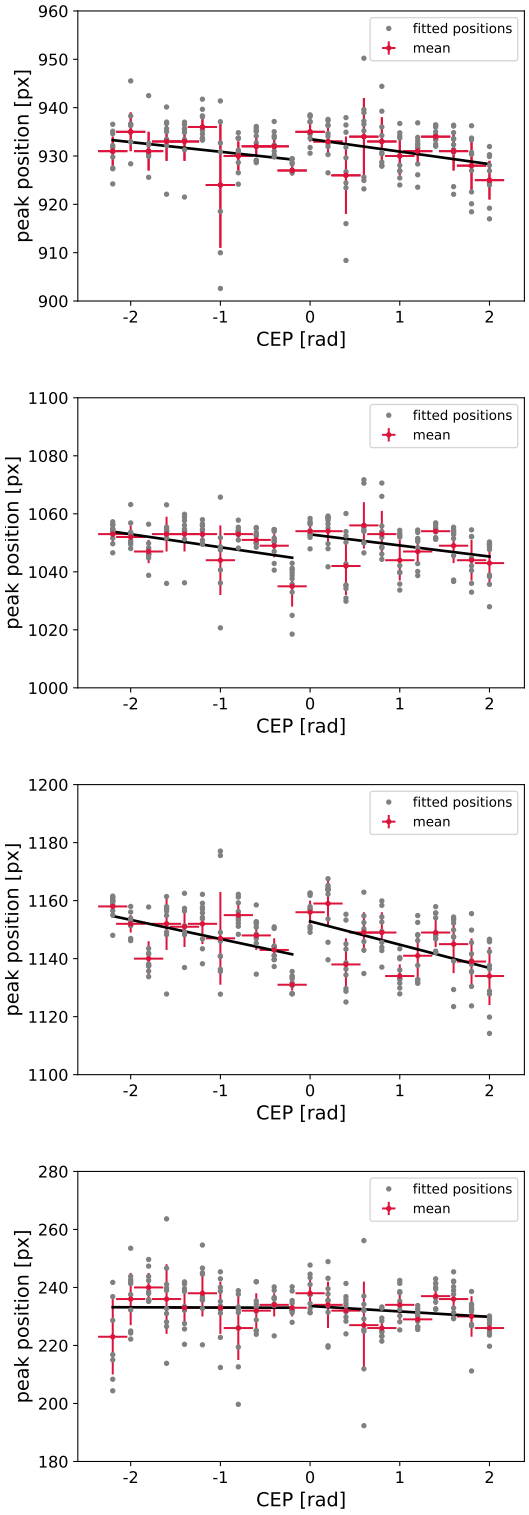

Figure 21: *The upper diagram shows the shift of the peaks with changing CEP for the left peak, the ones below for the middle peak and the right peak. The lowest plot shows the harmonic from the plateau region. The shift of the peak positions is clearly visible and gets more significant for higher harmonic orders.*

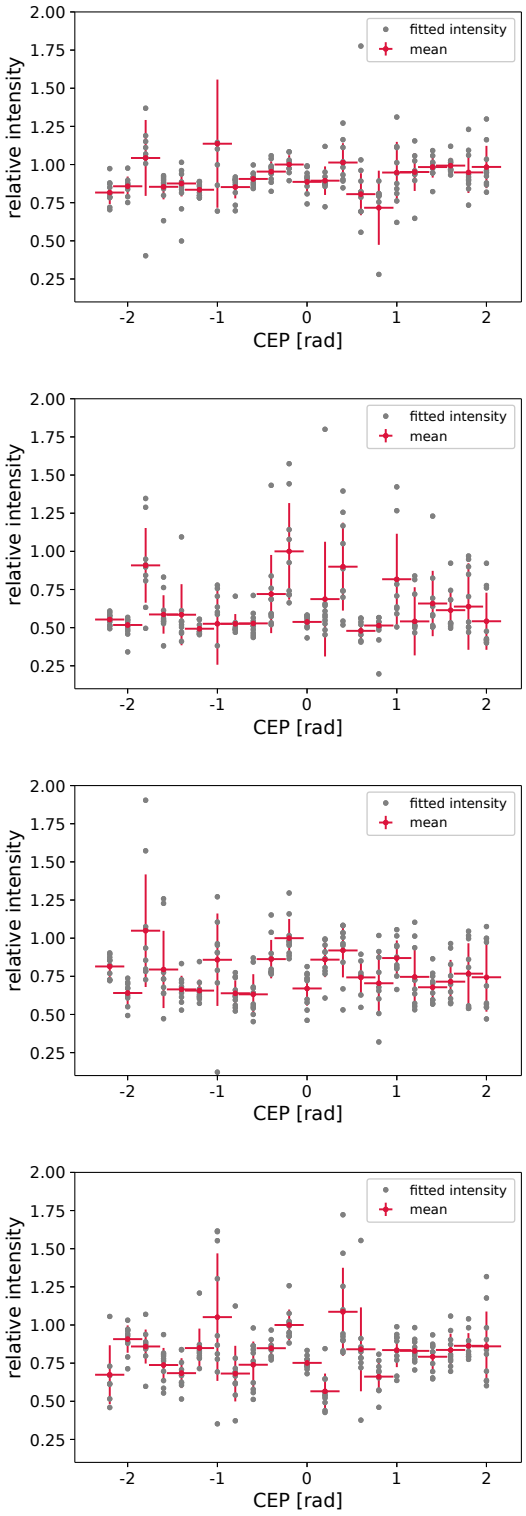

Figure 22: *The upper diagram shows the development of the intensity with changing CEP for the left peak, the ones below for the middle peak and right peak and the lowest one shows intensities for the harmonic in the plateau.*

approximate peak position [px]	σ [a.u.]
930	0.12
1050	0.09
1150	0.15
230	0.12

Table 2: *The standard deviation for the relative intensity of each peak was determined.*

give the impression that there is a factor that dominates the process and does not depend on the CEP so the relatively small changes actually produced by CEP-dependence are not visible.

5 Conclusions and Outlook

As a part of this thesis, a control loop to stabilize the carrier-envelope phase of ultrashort laser pulses has been established. The control of the CEP to a desired value with a standard deviation as low as 163 mrad will give the opportunity to do high precision spectroscopic experiments with a stable IR peak intensity.
Measurements of the CEP have been done for long and short femtosecond pulses, respectively without and with helium inside the hollow-core fiber, to show the naturally occuring changes in CEP and to regulate it. The attempt to find some good control parameters for the PI-control-loop was successful. These parameters can be used to regulate the CEP in future experiments. The spectral change of the IR-pulses over time was detected and evaluated. It was shown that helium inside the hollow-core fiber leads to a more stable spectrum in the wavelength range relevant for the detection of the CEP and indeed reduces fluctuations of φ_{CE}.
By observing the harmonic spectrum in dependence of the CEP, it was not possible to detect a change in intensity for the peaks in the cutoff region. A CEP-dependent energy shift, on the other hand, was clearly visible. With this, not only have previous experimental results been reproduced, but also has the functioning of the control loop been confirmed.
In the future, the new entrance window for the HHG-chamber, which was described in chapter 2, will be implemented to recreate the original beam path right before the chamber and to prevent effects caused by the additional insertion of glass. The active CEP-stabilization will enable transient-absorption spectroscopic experiments with CEP-stabilized femtosecond pulses and a constant harmonic spectrum in time.

6 Appendix

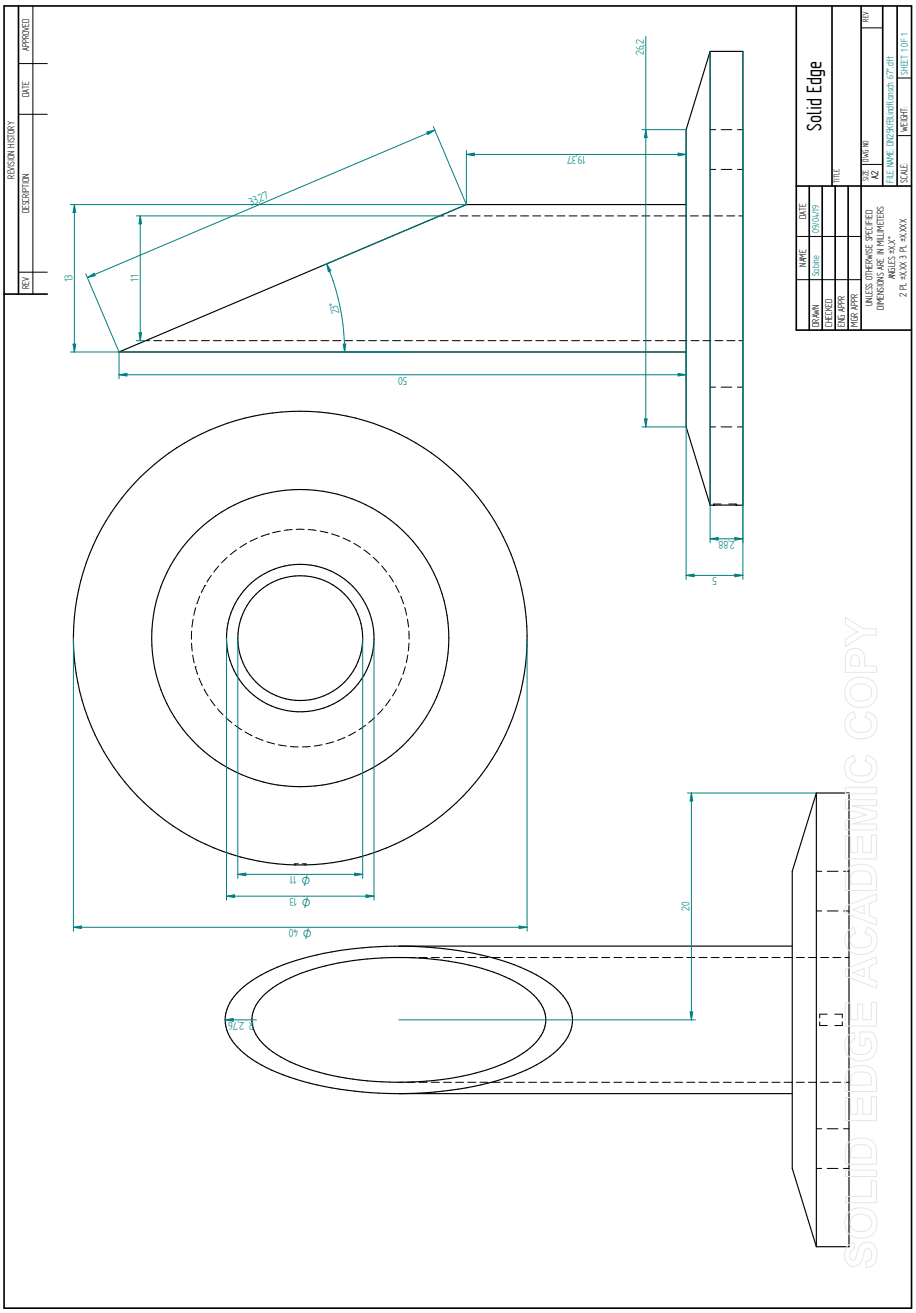

Figure 23: *Technical sketch of the entrance window redesigned to optimize the reflectance. More details are described in chapter 2.2.*

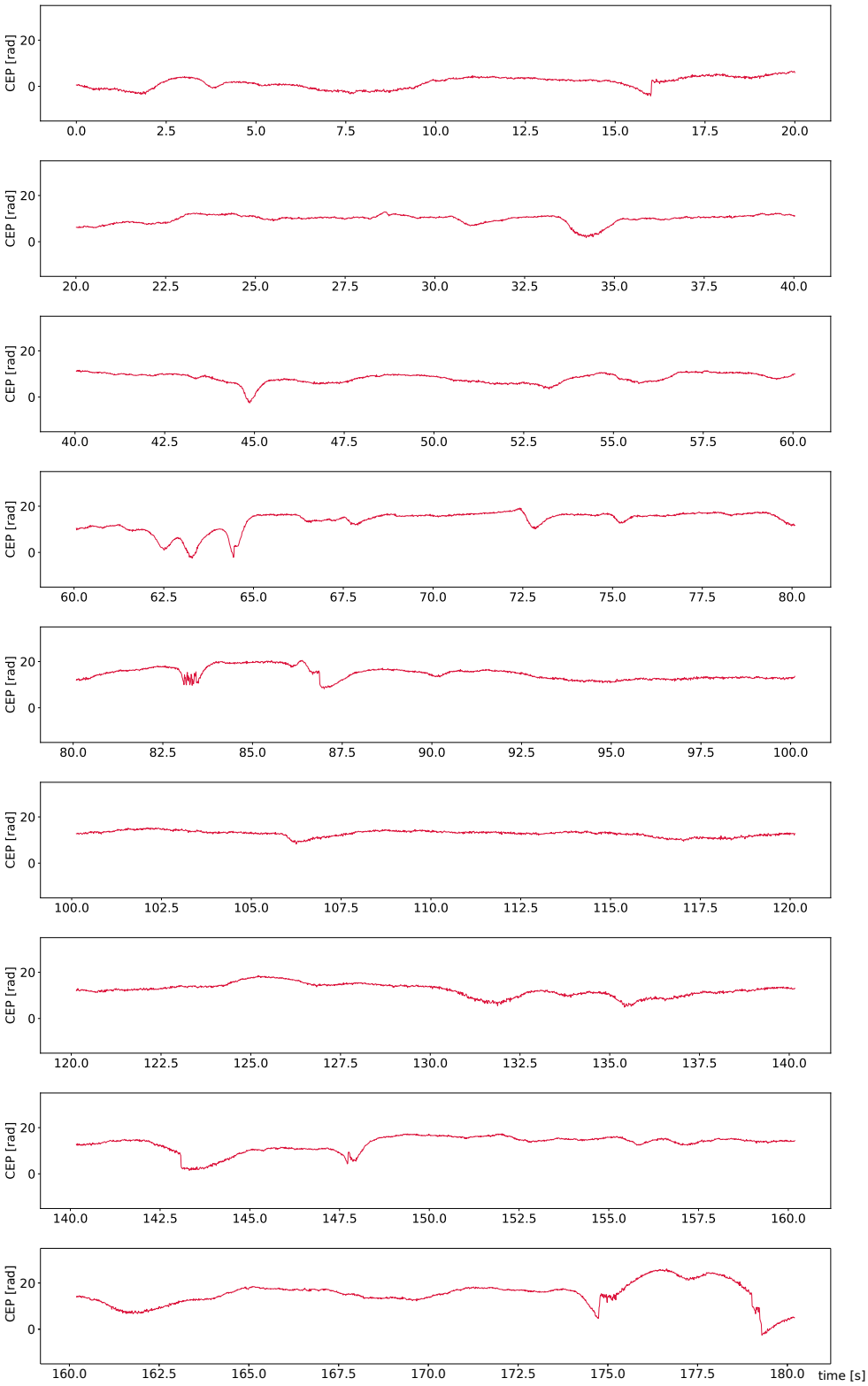

Figure 24: *A part of the long term measurement for short pulses. Details can be found in chapter 3.3.*

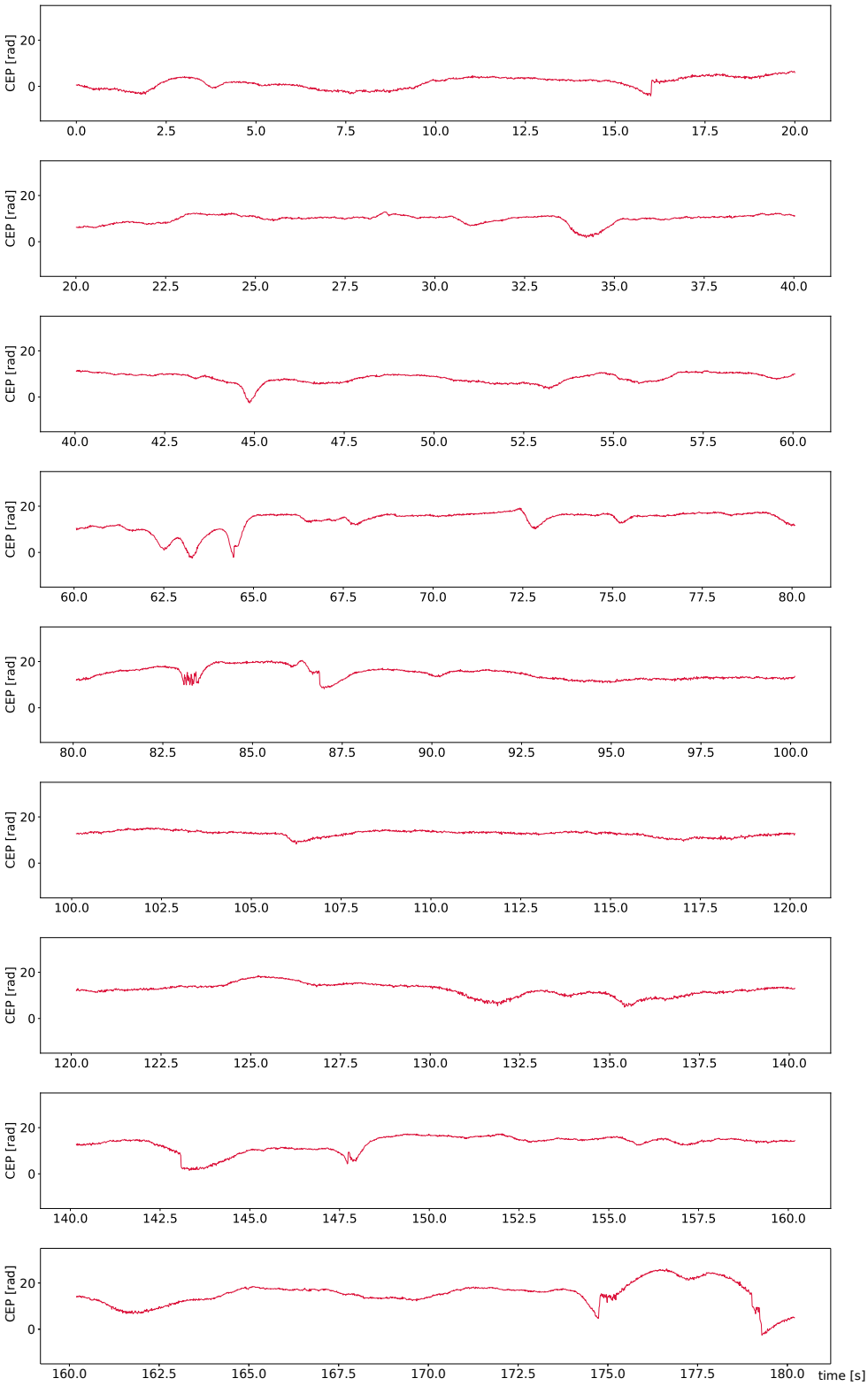

Figure 25: *A part of the long term measurement for short pulses. Details can be found in chapter 3.3.*

References

[1] Maximilian Hartmann. Characterization of few-cycle laser pulses. Master's thesis, Ruperto-Carola-University of Heidelberg, 2016.

[2] U. Keller F. Helbing, G. Steinmeyer. Carrier-envelope offset phase-locking with attosecond timing jitter. *IEEE Journal of Selected Topics in Quantum Electronics*, 9(4), 2003.

[3] Fabian Lücking. *Carrier-Envelope Phase Control for the Advancement of Attosecond Pulse Generation*. PhD thesis, Ludwigs-Maximilians-Universität München, 2014.

[4] Christopher J. Clark. Courtship dives of anna's hummingbird offer insights into flight performance limits. *Proceedings of the Royal Society B*, 276:3047–3052, 2009.

[5] Franziska Konitzer. Attosekundenspektroskopie. `https://www.weltderphysik.de/gebiet/teilchen/atome-und-molekuele/atome-und-quantenphysik/attosekundenspektroskopie/`, 2013. Retrieved September 2, 2019.

[6] Wolfgang Demtröder. *Laserspektroskopie - Grundlagen und Techniken*. Springer, 2007.

[7] Rüdiger Paschotta. Birefringence. `https://www.rp-photonics.com/birefringence.html`, Retrieved August 1, 2019.

[8] FEMTOLASERS Produktions GmbH. *CEPset^{TM} manual*, 2013.

[9] S. Kobayashi M. Takeda, H. Ina. Fourier-transform method of fringe-pattern analysis for computer-based topography and interferometry. *J. Opt. Soc. Am.*, 72(1), 1982.

[10] Kenichi L. Ishikawa. High-harmonic generation. `http://ishiken.free.fr/Publication/intech.pdf`, 2013. Retrieved September 2, 2019.

[11] M. Ivanov F. Krausz. Attosecond physics. *Reviews of Modern Physics*, 2009.

[12] F. Krausz T. Brabec. Intense few-cycle laser fields: Frontiers of nonlinear optics. *Reviews of Modern Physics*, 72(2), 2000.

[13] Sergej Neb. *Attosekunden-zeitaufgelöste Streaking-Spektroskopie an dem Schichtkristall Bi_2Te_3 und an den unterschiedlichen Oberflächen des nicht-zentrosymmetrischen Schichtkristalls BiTeCl*. PhD thesis, University Bielefeld, 2017.

[14] Veit Stooß. *Strong Field Spetroscopy: From Absorption to Time-Resolved Dynamics in Strong Fields*. PhD thesis, Ruperto-Carola-University of Heidelberg, 2018.

[15] A. Poppe T. Brabec F. Krausz T. W. Hänsch L. Xu, Ch. Spielmann. Route to phase control of ultrashort light pulses. *Optics letters*, 21(24), 1996.

[16] G.-Z. Yang Y. R. Shen. *Theory of Self-Phase Modulation and Spectral Broadening*, pages 1–32. Springer New York, 1989.

[17] G. Cerullo S. De Silvestri L. Gallmann G. Steinmeyer U. Keller M. Zavlani-Rossi, D. Polli. Few-optical-cycle laser pulses by opa: broadband chirped mirror compression and spider characterization. *Applied Physics B*, 2002.

[18] Wolfgang Demtröder. *Experimentalphysik 2 - Elektrizität und Optik*. Springer Spektrum, 2013.

[19] Wolfgang Bludau. *Lichtwellenleiter in Sensorik und optischer Nachrichtentechnik*. Springer, 1998.

[20] M. Salgado G. Goodwin, S. Graebe. *Control System Design*. Prentice Hall, 2000.

[21] FEMTOLASERS Produktions GmbH. *FEMTOPOWER^{TM} HE/HR CEP4 user manual*, 2016.

[22] S. Stagira M. Nisoli G. Sansone, C. Vozzi. Nonadiabatic quantum path analysis of high-order harmonic generation: Role of the carrier-envelope phase on short and long paths. *Physical Review A*, 70(013411), 2004.

[23] S. Stagira S. De Silvestri C. Vozzi M. Pascolini L. Poletto P. Villoresi G. Tondello M. Nisoli, G. Sansone. Effects of carrier-envelope phase differences of few-optical-cycle light pulses in single-shot high-order-harmonic spectra. *Physical Review letters*, 91(21), 2003.

[24] P. Raith A. Kaldun G. Sansone M. Krüger P. Hommelhoff Y. Patil Y. Zhang K. Meyer M. Laux T. Pfeifer C. Ott, M. Schönwald. Strong-field spectral interferometry using the carrierenvelope phase. *New Journal of Physics*, 2013.

[25] D. B. Milosevic B. Piraux A. de Bohan, P. Antoine. Phase-dependent harmonic emission with ultrashort laser pulses. *Physical review letters*, 81(9), 1998.

Acknowledgments

Mein Dank gilt

Prof. Dr. Thomas Pfeifer für die Möglichkeit, diese Arbeit in seiner Abteilung zu verfassen

PD Dr. Robert Moshammer für die Übernahme der Zweitkorrektur

Dr. Christian Ott für die Aufnahme in seine Arbeitsgruppe und die vielen Vorschläge für weiterführende Experimente

Paul Birk, **Gergana Borisova** und **Maximilian Hartmann** für die vielen Erklärungen, die Hilfe im Labor, das Korrekturlesen, das Beantworten meiner Fragen und generell für die große Unterstützung beim Erstellen dieser Arbeit

Der ganzen **Interatto**- und **X-Music**-Gruppe, nicht nur für die interessanten Einblicke in aktuelle Grundlagenforschung, sondern auch für die vielen Tischfußball-Spiele

Joris Edelmann, **Vivienne Leidel**, **Robert Meyer** und **Dominik Ostertag** für das Durchlesen meiner Arbeit und die Ideen zum Textsatz

Meiner Familie

Eigenständigkeitserklärung

Ich versichere, dass ich diese Arbeit selbstständig verfasst habe und keine anderen als die angegebenen Quellen und Hilfsmittel benutzt habe.

Heidelberg, den 5. September 2019 .....